Journal Pre-proofs

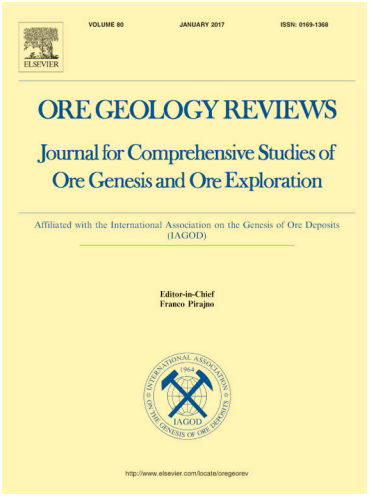

The Kirganik alkalic porphyry Cu-Au prospect in Kamchatka, Eastern Russia: A shoshonite-related, silica-undersaturated system in a Late Cretaceous island arc setting

Serguei G. Soloviev, Sergey G. Kryazhev, Vasily N. Shapovalenko, Gregory S. Collins, Svetlana S. Dvurechenskaya, Daria S. Bukhanova, Anton I. Ezhov, Konstantin I. Voskresensky

PII: S0169-1368(20)31078-7
DOI: https://doi.org/10.1016/j.oregeorev.2020.103893
Reference: OREGEO 103893

To appear in: *Ore Geology Reviews*

Received Date: 22 June 2020
Revised Date: 9 November 2020
Accepted Date: 17 November 2020

Please cite this article as: S.G. Soloviev, S.G. Kryazhev, V.N. Shapovalenko, G.S. Collins, S.S. Dvurechenskaya, D.S. Bukhanova, A.I. Ezhov, K.I. Voskresensky, The Kirganik alkalic porphyry Cu-Au prospect in Kamchatka, Eastern Russia: A shoshonite-related, silica-undersaturated system in a Late Cretaceous island arc setting, *Ore Geology Reviews* (2020), doi: https://doi.org/10.1016/j.oregeorev.2020.103893

The Kirganik alkalic porphyry Cu-Au prospect in Kamchatka, Eastern Russia: A shoshonite-related, silica-undersaturated system in a Late Cretaceous island arc setting

Serguei G. Soloviev*, Sergey G. Kryazhev, Vasily N. Shapovalenko***, Gregory S. Collins****, Svetlana S. Dvurechenskaya**, Daria S. Bukhanova*****, Anton I. Ezhov*, Konstantin I. Voskresensky***

**Institute of Geology of Ore Deposits, Petrography, Mineralogy and Geochemistry (IGEM), Russian Academy of Sciences, 35 Staromonetny Per., Moscow 109017, Russia*

***Central Research Institute of Geological Prospecting for Base and Precious Metals (TsNIGRI), 1-129 Warshawskoe Chaussee, Moscow 117545, Russia*

****RosGeologya Joint-Stock Company, 43-3 Khersonskaya St., Moscow 117246, Russia*

*****IG Copper, 94 Kalinina St., Khabarovsk 680000, Russia*

******Institute of Volcanology and Seismology, Russian Academy of Sciences - Far East Branch, 9 Piip Boulevard, Petropavlovsk-Kamchatsky 683006, Russia*

E-mail: serguei07@hotmail.com

Abstract

The Kirganik prospect is a silica-undersaturated, shoshonite-related, alkalic, porphyry Cu-Au system developed within the Upper Cretaceous island arc of Central Kamchatka. It is associated with a potassic volcano-plutonic suite of rocks that range from monzogabbro- and monzodiorite- to monzonite- and syenite-porphyry, followed by a second, compositionally overlapping magmatic cycle of trachytic syenite-porphyry, and possibly other, more differentiated monzonitic phases. The rocks exhibit a subduction-related, island arc rock affinity, with the magma generation involving low degree (~1-3 vol.%) partial melting of metasomatized, K-rich lithospheric mantle, followed by amphibole fractionation in a deep, probably lower crustal, magma chamber, with subsequent fractionation of accessory minerals, clinopyroxene and possibly biotite in shallower magma chambers. An early calc-potassic alteration assemblage of K feldspar-pyroxene-apatite-magnetite is closely related to small syenite intrusions. This stage is overprinted by more extensive potassic alteration zones of similarly quartz-free biotite-K feldspar-magnetite, some of which contain abundant Cu-sulfides (mostly bornite and chalcopyrite, with minor chalcocite), minor native gold and PGE minerals. Subsequent sodic-potassic to calcic-sodic-potassic alteration comprising albite-magnetite-calcite-epidote, and propylitic assemblages of chlorite-magnetite-epidote±pyrite are much more weakly developed. These hydrothermal alteration assemblages form lens-shaped, replacement-style zones, rather than stockworks of well-defined veinlets/stringers, particularly quartz-sulfide veinlets, which are absent. Apatite from calc-potassic and potassic alteration assemblages contains low salinity (5-10 wt.% NaCl-eq.) liquid-gaseous fluid inclusions indicating a homogenous, low salinity, supercritical aqueous fluid exsolved directly from a cooling and degassing pluton, with no boiling and unmixing into hypersaline and gaseous phases. Under inferred high temperatures of calc-potassic and potassic alteration (450-550 to 400-420^{o}C) and significant (2.1-2.2 to 1.5-1.8 kbar) pressure, this suggests a deep (>5 km ?), possibly root-level of a larger, shallower, since eroded, porphyry Cu-Au system. The current geological setting and distribution of alteration and mineralization can be explained by a sharp, up to 90°, post-mineral tilting of the initial narrow, subvertical, 'finger-like' intrusions and related mineralized system, followed by deep exhumation. As a consequence, a significant part (>1.5 km) of the deep porphyry system is currently exposed at surface.

Keywords: copper; gold; porphyry; shoshonite; Kamchatka; Russia

1. Introduction

Alkalic magmatic-hydrothermal systems related to high-K calc-alkaline to shoshonitic igneous suites are important in producing significant porphyry Cu-Au to Cu-Au-Mo and epithermal Au deposits (Mutschler and Mooney, 1993; Richards, 1995; Jensen and Barton, 2000; Sillitoe, 2002; Soloviev, 2014; Muller and Groves, 2019). Many notable examples of such systems are known in the Northeast and Southwest Pacific, where they comprise large porphyry Cu-Au deposits (e.g., Lang et al., 1993, 1995; Holliday et al., 2002; Wilson et al., 2003; Pollard et al., 2005; Lickfold et al., 2007; Cooke et al., 2007; Redmond and Einaudi, 2010; Bissig and Cooke, 2014). In contrast, little is known about alkalic porphyry Cu-Au systems in the northwestern (Russian) part of the Circum-Pacific region, although they represent a viable part of porphyry Cu-Au mineralization there, together with porphyry Cu-Au deposits of the calc-alkaline type (e.g., Mihalaisky et al., 2015; Soloviev et al., 2019a). In particular, until most recently, only the world-class Peschanka Cu-Au-Mo porphyry deposit in Chukotka Peninsula was described as an example of the alkalic Cu-Au porphyry type in a subduction-related setting (e.g., Soloviev, 2014; Muller and Groves, 2019). A recent publication on the Lazurnoe porphyry Cu-Au-Mo deposit in the Sikhote-Alin highlighted its relationships to shoshonitic rocks in a transform plate margin-related to post-collisional tectonic setting (Soloviev et al., 2019b). These publications have demonstrated a diversity of tectonic and metallogenic settings of porphyry Cu-Au deposits in the Northwest Pacific, comprising numerous subduction-related and post-subduction magmatic arcs (e.g., Nokleberg et al., 1998; Yakubchuk, 2009).

The Kirganik prospect is a silica-undersaturated (cf. Lang et al., 1993, 1995) alkalic porphyry Cu-Au system related to a Late Cretaceous (to Paleocene ?) shoshonitic volcanic-plutonic suite in Central Kamchatka. Copper and gold mineralization at Kirganik was discovered in 1957-1958 (I.N.Ilchenko, A.I.Baikov) and explored during several exploration programs by trenching and limited drilling, particularly in 1959-1962 and the late 1970s-early 1980s (E.K.Ignatiev, A.S.Gumovsky, P.P.Usatyuk, A.L.Basharkevich). Based on this, the prospect resources were estimated at 0.9 Mt of contained Cu and 92 t Au (averaging 0.7% to 0.5% Cu and 0.75 g/t to 0.5 g/t Au for various resource blocks and categories; Gumovsky et al., 1984). Concurrently, igneous rocks and hydrothermal alteration styles were studied (e.g., Flerov and Koloskov, 1976; Vlasov and Vasilevsky, 1964; Polokhov and Volynets, 1968; Zvezdov, 1997). In the late 1990s-early 2000s, the prospect was evaluated by BHP-Billiton, and its resources were estimated at 255 Mt averaging 0.34% Cu and 0.12 g/t Au (equal to 0.9 Mt Cu and 33 t Au); minor Pt and Pd

mineralization was also reported (Ignatiev et al., 1999). However, these resource figures may not represent the prospect true size, as the most recent drilling revealed "the lack of sizeable porphyry zones to a depth of at least 500 m from the surface" (e.g., "Development Strategy…", 2017). The present paper is focused on the new geological, petrologic, and fluid inclusion data to provide a more detailed view on the prospect formation.

2. Regional tectonic and metallogenic setting

The Kamchatka Peninsula (Fig. 1) comprises a metamorphic basement terrane that is surrounded and partially overthrusted by accreted Mesozoic and Cenozoic island arc and turbidite terranes, in turn overlain by younger Cenozoic sedimentary basins and subaerial volcanic belts (Nokleberg et al., 1998). These terranes are parts of the Kamchatka-Aleutian collage with a westward convergence along the Pacific margin, representing a complexly deformed double arc-backarc system that developed along the westward subducting Pacific plate (Yakubchuk, 2009). The double arc-backarc may have been the result of intra-arc spreading, or alternatively, the accretion of another external arc was suggested (Nokleberg et al., 1998; Yakubchuk, 2009). There have been several episodes of intense magmatic activity during this complex evolution, with the respective magmatic arcs likely marking subduction zones of various ages. Correspondingly, several episodes of shoshonitic magmatism in Kamchatka are distinguished, including those occurring during the Late Cretaceous-Paleocene, Neogene, and Quaternary. Whereas the early episodes are related to the respective subduction processes, the late episodes can represent both subduction-related and post-subduction settings (Tsvetkov et al., 1993; Kepezhinskas, 1994; Koloskov et al., 1999; Flerov et al., 2001; Flerov and Seliverstov, 2008; Fedorov et al., 2013; Perepelov, 2014).

Due to the presence of numerous magmatic arcs, Kamchatka is considered a highly fertile region for various styles of mineralization. Three major styles are most widespread. Firstly, there is Cu-Ni sulfide (+Co, PGE) mineralization associated with ophiolites and/or mafic-ultramafic (gabbro-norite-peridotite, norite-cortlandite, etc.) intrusions and related volcanic (picrite, dolerite, basalt) rocks (e.g., Shanuch deposit; Konnikov et al., 2006). Based on the U-Pb zircon geochronology, Slyadnev et al. (2006) distinguished two major epochs of this style of mineralization - Late Cretaceous (78±2 Ma) and Eocene (48±3 Ma).

Secondly, the Kamchatka Peninsula hosts numerous occurrences of porphyry-style Cu-Au mineralization (Fig. 1). The majority of these occur in an extended belt that can be traced intermittently along the Central

Kamchatka peninsula, although similar mineralization is also known elsewhere in the region. Two main metallogenic epochs can be distinguished, (1) the early (Late Cretaceous-Paleocene ?) porphyry Cu-Au mineralization related to the high-K calc-alkaline to shoshonitic igneous suites, and (2) the late (Oligocene-Neogene) porphyry Cu-Au±Mo mineralization related to medium-K calc-alkaline (including adakitic) igneous suites. As a result, both alkalic and calc-alkaline types of porphyry Cu-Au mineralization are present and locally superimposed within the same district-scale to local structures.

Finally, and currently most important from an economic perspective, the region hosts numerous Neogene to Quaternary epithermal Au to Au-Ag and Au-Hg deposits and occurrences (e.g., Nokleberg et al., 1996; Yakubchuk, 2009; Goryachev et al., 2010; Goryachev and Pirajno, 2014) (Fig. 1). Goryachev et al. (2010) distinguished three main metallogenic belts, the Western, Central and Eastern Kamchatka Gold Belts. The Western belt comprises Au (including the large Amethystovoe Au deposit) and minor Ag, Hg and Sn mineralization and is associated with the Eocene to Oligocene rhyolite-dacite-andesite volcanics, and extends intermittently along the west Kamchatka coast. The Central Kamchatka Gold Belt comprises the majority of large Au to Au-Ag (with abundant Te-Bi mineralization) deposits associated with Paleogene-Neogene andesite and andesite-basalt volcanics and can be traced for over 1800 km. This belt also partially overlaps with the main porphyry Cu-Au belt. In addition to Au and Au-Ag mineralization, Hg and Au-Hg occurrences are present. The Eastern belt consists of Au-Ag mineralization (including the Kumroch deposit) associated with Pliocene to Quaternary volcanics, and extends from South Kamchatka to the junction with the Aleutian island arc (Fig. 1; Goryachev et al., 2010).

3. District geology and mineralization

The Kirganik prospect is situated in the multi-metal Central Kamchatka mineral district, part of the Central Kamchatka Gold Belt (Figs. 1, 2). In this region, packages of allochthonous tectonic slices comprising Paleozoic and Mesozoic-Paleocene island arc terranes (likely marking variously-aged subduction zones) were thrust westward over flysh and turbidite sequences, themselves overlying a high-metamorphic pre-Cretaceous (?) basement terrane (e.g., Slyadnev et al., 2006). The Mesozoic-Paleocene island arc terranes include the Late Cretaceous Irunei (Irunei-Ganaly) terrane, which is underlain by a metamorphic basement and Lower to Upper Cretaceous metaterrigenous and metaterrigenous-volcanic sequences some 600 m thick (Slyadnev et al., 2006).

These sequences are overthrusted by the Upper Cretaceous Irunei sequence (3000 m thick) comprising a lower unit of chert, tuffaceous siltstone, tuffite, minor basalt, andesite-basalt and their tuffs, and an upper unit of basaltic to andesite-basalt and trachybasalt lavas and tuffs, tuffaceous siltstone, sandstone, and chert. This succession is overlain by the Upper Cretaceous (to Paleocene ?) Kirganik sequence (3000 m thick) that comprises lavas and tuffs of potassic trachybasalt and basalt, minor tranchyandesite, absarokite, shoshonite, leucite tephrite, and analcime basalt, as well as tuffaceous sandstone, siltstone, gravelite, tuffite, and turbidite/mixtite (Koloskov et al., 2009). Fedorov and Dubik (1990) interpreted the volcanic rocks to have subduction-related geochemical signatures, with depletion in Ta and Nb reflecting partial melting of a mantle source (possibly garnet-spinel lherzolite), whilst isotopic ratios of $\varepsilon Nd(T)=8.2\text{-}9.7$ and $^{87}Sr/^{86}Sr=0.70316\text{-}0.70371$ indicate no crustal contamination occurred.

These sequences were intruded by several volcanic-plutonic and plutonic suites. The Early Cretaceous (125 to 111 Ma dated using the K-Ar method; Slyadnev et al., 2006) plagiogranite intrusions are considered the earliest, followed by the Late Cretaceous (89.5 to 57 Ma using the K-Ar method to 80±2 Ma using U-Pb of zircons; Slyadnev et al., 2006) diorite-plagiogranite-granodiorite intrusions. A younger (Eocene - 49.2±0.2 Ma; Stepanov and Trukhin, 2007) gabbro-pyroxenite-peridotite suite is represented by small stocks that are accompanied by Cu-Ni sulfide (+Co, PGE) mineralization (Konnikov et al., 2006).

A Late Cretaceous (to Paleocene ?), subvolcanic to hypabyssal igneous suite is coeval with the early (older) porphyry Cu-Au mineralization. It comprises monzogabbro (“shonkinite” and “essexite”), monzonite and syenite, and makes up the Kirganik potassic (shoshonitic) suite, which can be correlated with the high-K volcanic rocks of the Upper Cretaceous-Paleocene Kirganik volcanic sequence (e.g., Fedorov and Dubik, 1990; Fedorov et al., 2013). These comagmatic potassic rocks can be traced along a narrow (20-25 km) intermittent “strip” for >140 km north-south, and are associated with small domes and grabens (Flerov and Koloskov, 1976; Flerov et al., 2001). Isotopic ages for these rocks vary, with K-Ar dating returning 86 to 52 Ma, whereas U-Pb zircon ages of syenite returned 70.4±0.7 Ma to 63.0±0.6 Ma (Slyadnev et al., 2006; Hourigan et al., 2004). Both high- and low-Ti varieties are present among these potassic rocks in Central Kamchatka (e.g., Flerov et al., 2001).

Several younger (Late Oligocene to Miocene to Quaternary) plutonic and volcanic-plutonic suites of magnetite-series (after Ishihara, 1981) diorite, granodiorite and granite intrusions occur in the Central Kamchatka Gold Belt. In particular, a Late Oligocene to Miocene age (21 to 15 Ma using the K-Ar method; Slyadnev et al.,

2006) was determined for the Lavkin diorite-granodiorite-granite suite. This suite is one of the coeval plutonic to volcanic-plutonic suites that define the younger regional porphyry Cu-Au±Mo mineralization trend of the Central Kamchatka Gold Belt. A Miocene, Miocene-Pliocene, or Pliocene-Quaternary age was determined for volcanic-plutonic (diorite-granodiorite to andesite-dacite) suites that are associated with examples of the regional epithermal Au to Au-Ag deposit trend which occur within the district (e.g., Aginskoe, Ogancha, Sukhariki, etc.; Fig. 2).

The Kirganik (Khim-Kirganik) mineralized cluster is part of the Central Kamchatka district and comprises the Kirganik porphyry Cu-Au prospect and other porphyry Cu-Au occurrences related to the Late Cretaceous (to Paleocene ?) Kirganik potassic (shoshonitic) suite. The cluster is associated with an eroded stratovolcano some 20 km in diameter, which is complicated by radial and concentric faults defining variously-sized structural blocks (Fig. 2; e.g., Zvezdov, 1997). The structure is composed of the Upper Cretaceous-Paleocene volcanic-sedimentary rocks, which evolve from lavas, lavabreccias, clastolavas, and agglomerate tuffs to volcanic-sedimentary facies. Smaller (satellitic) dome-like structures controlling porphyry Cu-Au occurrences complicate the main stratovolcano and are associated with separate groups of dikes, sills, and small subvolcanic stocks of monzogabbro, monzodiorite, syenite and other potassic rocks. Part of this structure was destroyed by the Late Oligocene-Miocene diorite-granodiorite plutons and numerous dikes related to these plutons. These younger intrusions are accompanied by porphyry Cu-Au-Mo occurrences representing a younger phase of porphyry mineralization. Gold (Au-Ag) mineralization possibly related to the Miocene-Quaternary (?) igneous suites is also present (Fig. 2).

4. Prospect geology

The geological setting of the Kirganik prospect remains controversial. In particular, the volcanic-sedimentary sequence was previously thought to have flat-lying to gently dipping bedding over the central part of the prospect area, with a gradual increase in dip toward its periphery, thus representing an almost undisturbed local volcanic dome. However, as demonstrated by Ignatiev et al. (1999), the volcanic-sedimentary rocks form a north- to northeast-striking monocline, with older rocks in the southeastern part of the prospect, and younger rocks to the northwest, all dipping at 50° to 80° to northwest (Fig. 3). Further controversy exists in the interpretation of age and the composition of the volcanic-sedimentary sequence hosting the mineralization. Whereas earlier authors assigned it to the younger Kirganik sequence, Ignatiev et al. (1999) suggested that it belongs to the older and less alkaline

Irunei volcanic-sedimentary sequence, as no primarily high-K volcanic rocks are observed. Furthermore, in contrast to some authors, who distinguished a large "shonkinite" (monzogabbro) intrusion at the prospect, together with high-K volcanic rocks, we observed only small dikes/sills of mafic alkaline rocks, whereas the rest of the pyroxene-biotite-K-feldspar rocks (previously assigned to the "shonkinite") represent a halo of very intense calc-potassic (pyroxene-K-feldspar-dominant) and potassic (biotite-K-feldspar-dominant) alteration. As a result, most of the volcanic-sedimentary rocks, as well as dikes/sills, in the central part of the prospect appear to have been partially to almost completely altered, with the development of hydrothermal (principally calc-potassic to potassic) replacement-style alteration zones within a nearly isometric area ~1.5 km by 1.5 km across.

Within this area, at least five lens-shaped to lenticular, pinching-and-swelling, zones of Cu-Au mineralization (at 0.1% Cu cut-off) outcrop at the surface, with the largest mineralized exposure extending for ~1250 m north-south and attaining a width of ~200 m (Fig. 3). Altered but almost barren rocks separate these outcropping mineralized zones. We interpret these mineralized outcrops as representing an eroded surface expression of a single flat-lying, ~1.2x1 km mineralized zone, which repeatedly plunges and rises, with "ridges" and "valleys", thus alternating with barren intervals on the surface (Fig. 4). Its thickness varies from several meters to 100-150 m, with significant Cu and Au grades over wide intervals exposed by trenching and drilling (Fig. 4). Gold grades are typically 0.1-1 g/t; grades of up to 5% Cu, 16.2 g/t Au, 22 g/t Ag, 0.8 g/t Pt and 1.0 g/t Pd were reported in the more local intervals, whereas grades up to 63 g/t Au, 7.70 g/t Pd and 0.35 g/t Pt were returned in surface grab samples (Ignatiev et al., 1999). A 500 kg metallurgical sample collected from this zone averaged 0.76% Cu, 0.3 g/t Au and 2.4 g/t Ag (Slyadnev et al., 2006). Other, possibly subparalleling but much smaller mineralized zones alternating with wider barren intervals are present below the main mineralized zone. These generally flat-lying to shallow-dipping mineralized zones are roughly paralleling intrusions, which appear to be also subhorizontal (Fig. 4). Some deeper drill holes passed through the mineralized intrusions and associated zones of potassic alteration and mineralization, entering less altered rock at depth, together with zones of propylitic alteration. A larger porphyry intrusion was not encountered to a drilled depth of ~500 m (Fig. 4).

Bornite and chalcopyrite, with minor chalcocite, occur as part of a potassic (biotite-K-feldspar-magnetite) alteration assemblage(s), whereas other similarly altered rocks contain trace to no mineralization. Cu sulfides (2-5 to 20-30 vol.% in intervals >0.1% Cu) have an irregular, patchy distribution, typically in the form of small local

lenses, “pods”, blebs, dense to weak fine (1-3 mm) to coarse (10-20 mm) interstitial dissemination, whereas quartz-sulfide veinlets are absent. Vlasov and Vasilevsky (1964) reported massive bornite lenses up to 80 cm thick and 1.2 m long. Minor chalcopyrite is associated with an inner zone (cf. Corbett, 2017) of propylitic alteration characterized by an assemblage of epidote-chlorite-calcite-albite-magnetite. This mineralization occurs as small, up to 1-2 m wide, isolated intervals within the potassic alteration “core”. A much wider, outer chlorite-dominant propylitic alteration zone that is hundreds of meters wide, is found peripheral to the potassic alteration “core” and at greater depth. It contains trace chalcopyrite and/or trace to abundant pyrite (Fig. 4).

Numerous Late Oligocene-Miocene dikes of diorite-porphyry, quartz diorite-porphyry, and granodiorite-porphyry are mostly fresh and barren, and only locally are subjected to phyllic and/or argillic alteration. These dikes as well as linear zones of phyllic and argillic alteration trace post-mineral faults that possibly displace and truncate mineralized zones. These linear zones are moderately- to steeply-dipping, up to 40 m wide, and extend up to 1 km along strike (Fig. 4). They typically contain trace Cu, but locally carry high Au grades.

5. Analytical methods

The analyses of igneous rocks were performed in the TsNIGRI Labs, Moscow. SiO_2, TiO_2, Al_2O_3, $Fe_2O_{3\ total}$, MnO, MgO, CaO, K_2O, and P_2O_5, were determined by X-ray fluorescence method. FeO was determined by a wet chemical method (volumetric titration). Powdered samples were analyzed by ICP-MS method for trace elements. Analytical errors are 0.5-5% for major elements and 1-10% for trace elements, depending on the concentrations. The EPMA analyses of minerals were performed in the IGEM RAS, Moscow, using a JXA-8200 (Jeol) electron probe microanalyser, under operating conditions of 20 kV accelerating voltage, 20 nA beam current, with a beam diameter ~3 μm. The accuracy of element measurements was $\pm$2% rel. for concentrations >10 wt.%, $\pm$5% rel. for concentrations of 5-10 wt.%, $\pm$10% rel. for concentrations of 1-5 wt.%, and $\pm$15% rel. for concentrations of 0.1-1.0 wt.%.

The Rb–Sr isotope analyses were performed in the GEOKHI RAS, Moscow. The 20-30 mg handpicked and cleaned mineral samples were dissolved and decomposed by HF-HNO_3 solution (5:1) with ^{85}Rb + ^{84}Sr mixture diluent during 3 days under permanent mixing in teflon cups. The dry precipitate was converted into a chloride form by triple evaporation in concentrated HCl, and Rb and Sr were separated and purified by the ion-chromatography method. The Sr isotope composition and Rb and Sr concentrations were measured using the multi-collector Triton mass-spectrometer. Measurements for the American Standard Reference Material NBS 987 Sr standard yielded $^{87}Sr/^{86}Sr = 0.710245\pm0.000011$ ($2\sigma_{av.}$, N=13). Regression

and age calculations of isochrons were performed using Isoplot/Ex Version 3.0 software (Ludwig, 2003). The errors for the $^{87}Rb/^{86}Sr$ and $^{87}Sr/^{86}Sr$ ratios at a confidence level of 95% were 1% and 0.006%, respectively.

Fluid inclusions were studied in samples from surface outcrops and drill core. Twenty seven doubly polished sections of 0.3 to 0.5 mm thick were prepared from 20 individual samples for fluid inclusion petrography and microthermometry. The fluid inclusion study was focused on fluid inclusion assemblages (FIA) of closely associated groups or trails of fluid inclusions with visually similar phase ratios and shapes (Goldstein and Reynolds, 1994). The sequence of entrapment can be inferred from observations of crosscutting trails of FIA along individual fractures or rare primary inclusions distributed randomly within the core of crystals or pseudosecondary trails that are associated with healed microfractures terminated by crystal growth zones (Roedder, 1984). This also enables linking groups of fluid inclusions to various mineralizing stages based on their absence in younger mineral assemblages (Masterman et al., 2005).

Microthermometric analyses were made using the UMTK-3 freezing-heating stage designed by VIMS Institute and modified by TsNIGRI Institute, to allow low-temperature experiments. Low-temperature measurements were conducted first; cooling was by liquid N_2 flow. The stage employs a chromel-alumel thermocouple and is capable of attaining temperatures ranging from below −180 to over +650 °C. The stage was periodically calibrated using the boiling temperature of pure N_2 (−196 °C), triple point for pure CO_2 (−56.6 °C), temperatures of ice melting in standard NaCl solutions (from −18° to −1°C), melting temperatures of $AgNO_3$ (210°C), K_2CrO_7 (398°C), and NaI (651°C). Final ice-melting temperatures were accurate to ±0.2°C, eutectic temperatures to ±1.5°C, and homogenization temperatures to ±5°C. The heating rate (at above 30°C) was 5°C/min up to a heating limit at 650°C.

6. Igneous rocks of the Late Cretaceous (to Paleocene ?) potassic volcanic-plutonic suite

The igneous rocks assigned to the Kirganik suite (cf. Fedorov and Dubik, 1990; Fedorov et al., 2013) in the prospect area comprise several porphyry to almost equigranular varieties (monzogabbro-porphyry, monzodiorite-, monzonite-, and syenite-porphyry, etc.) (Table 1). In particular, monzogabbro-porphyry (Fig. 5A) is a mafic rock (60-75 vol.% of mafic minerals, principally clinopyroxene and minor biotite), with small phenocrysts of clinopyroxene (25-40 vol.%), rarely K-feldspar and/or plagioclase. A younger biotite-pyroxene to biotite-pyroxene-amphibole monzodiorite-porphyry contains 40-50 vol.% of mafic minerals (Fig. 5B). Monzonite-porphyry contains 30-40 vol.% of mafic minerals (pyroxene, amphibole, and biotite), dominant plagioclase, and minor K-feldspar (Fig. 5C). All these rocks are subjected to calc-potassic and potassic alteration (Fig. 5D). Other, younger, typically finer-grained monzonitic rocks appear to be forming small dikes, which contain xenoliths of K-

feldspar-dominant metasomatites with or without Cu-sulfides (Fig. 5E-G); the rocks are also subjected to potassic alteration, with bornite and/or chalcopyrite, thus representing intramineral intrusions.

Syenite to syenite-porphyry forms small vein-like intrusions typically <1 m thick (rarely up to 2-3 m thick) and is a leucocratic fine- to coarse-grained, locally K-feldspar-phyric rock composed of dominant (75-90 vol.%) tabular K-feldspar, with minor (10-25 vol.%) mafic minerals (clinopyroxene and amphibole, rarely biotite). The rock is characterized by unstable composition and varies from that with fine-grained equigranular texture to blocky almost monomineralic K-feldspar aggregates (Fig. 5H-I). Larger dikes/veins evolve into stockworks of dikelets or microdikes ("vein-dikes", after Seedorff et al., 2005) varying from 3-5 mm to 10-20 mm in thickness, and are surrounded by wider fenite-like halos of exocontact magmatic replacement in the form of porphyroblastic K-feldspar and branching monomineralic K-feldspar "injections" (Fig. 5I). Minor clast- to matrix-supported magmatic breccia is present, with syenite matrix and angular fragments of volcanic and mafic intrusive rocks (Fig. 5J). It appears that syenite intrusions occur in the focus of the most intense calc-potassic alteration, where they are partially to entirely converted into (or evolve to ?) pyroxene-orthoclase aggregates with magnetite and apatite.

A younger intrusive phase is represented by trachytic syenite-porphyry (to phonotephrite-porphyry ?). This K-feldspar-phyric rock differs from the older rocks by sharp porphyritic appearance, with minor (~10-20 vol.%) to abundant (>80 vol.%) elongated, "noodle-like" orthoclase phenocrysts, locally with a flow texture (Fig. 5K). The quantity of orthoclase phenocrysts changes gradually to abruptly, the latter suggesting multiple intrusions (Fig. 5L). The rock crosscuts syenite and zones of potassic alteration (Fig. 5M-N). Xenoliths of rocks subjected to intense potassic alteration with bornite are present in trachytic syenite-porphyry (Fig. 5O); the latter is subjected to reddening (hematite dusting) of K-feldspar and is overprinted by propylitic alteration.

The rocks petrographically exhibiting the least altered signatures, together with the low (<2 wt.%) LOI, and satisfying the criterion of essential immobility of Al and Ti (Fig. 6A), the latter supporting their least altered nature (MacLean and Barrett, 1993), were selected to characterize the igneous geochemistry (Table 2). Although this dataset may not include the entire spectrum of igneous rocks existing at the prospect, it highlights a magmatic differentiation trend, ranging from ~43 wt.% SiO_2 to ~60 wt.% SiO_2; this trend is partially overlapped by younger, more primitive trachytic syenite-porphyry compositions, thus suggesting a cyclic magmatic differentiation (Fig. 6B). On the total alkalis vs. SiO_2 diagram (Fig. 6B), the rocks plot mostly in the alkaline field. The rocks plot in the

shoshonitic field (Fig. 6C), and are strongly metaluminous (Fig. 6D). Consistent with the presence of accessory magnetite, the Fe_2O_3/FeO ratio is >0.4 in all rock varieties, thus indicating oxidized (magnetite series; Ishihara, 1981) intrusions. The discrimination diagram of Muller and Groves (2019) designed for potassic igneous rocks (Fig. 6E) indicates the subduction-related affinity of the rocks. The Nb/Zr vs. Zr diagram of Thieblemont and Tegyey (1994) supports the subduction-related affinity (Fig. 6F). Some rocks bear elevated Ti contents, whereas the majority belong to the low-Ti (<1 wt. % TiO_2) shoshonitic type (cf. Kepezhinskas, 1994); no high-Ti igneous rocks have been encountered in this study, although they may be present in the prospect area (e.g., Flerov et al., 2001). In primitive mantle-normalized trace element spider diagrams (Fig. 6G), the rocks, particularly the early intrusive phases, display strong negative Nb, Ta, and Zr anomalies, consistent with the subduction-related origin; however, Ta and Zr deficits become weaker toward later phases. Strong positive K, Sr, Ba, Rb, and P anomalies and a weak negative Ti anomaly are also recorded. Chondrite-normalized REE diagrams (Fig. 6G) indicate a shallow-differentiated REE pattern, with a moderate enrichment in LREE and no Eu anomalies.

7. Hydrothermal assemblages and mineralization

The hydrothermal mineral paragenesis at Kirganik includes potassic, propylitic, phyllic, and argillic alteration assemblages (Fig. 7). Potassic alteration by its intensity absolutely dominates over the other alteration types, and likely includes several substages (e.g., calc-potassic, potassic, and sodic-potassic). Propylitic alteration occurs both within and outside the contour of potassic alteration. Zones of potassic and propylitic alteration are cut by the Late Oligocene-Miocene diorite-porphyry dikes, which are subjected to phyllic and argillic alteration.

7.1 Potassic (including calc-potassic to sodic-potassic) alteration

This alteration occurs in the central (core) part of the prospect-scale alteration halo, where it overprints stocks of monzogabbro-, monzodiorite- and monzonite-porphyry, and adjacent volcanic-sedimentary rocks. Potassic alteration assemblages form coarse- to fine-grained lens-shaped aggregates, with indistinct margins, anastomosing, branching and coalescing veins and veinlets (resembling A-type veins, after Gustafson and Hunt, 1975), zones of pervasive replacement and “flooding”, coarse to fine dissemination, and patchy accumulations, rather than stockworks of well-defined veinlets/stringers. Several partially overlapping mineral types of potassic

329 alteration occur, with variable contents of biotite, K-feldspar, pyroxene, apatite, albite, magnetite, and Cu-sulfides.
330 Quartz is absent in potassic alteration assemblages at Kirganik.

331 The earliest potassic substage, calc-potassic alteration, comprises an assemblage that includes pyroxene,
332 white to light-grey K-feldspar (orthoclase), minor brown Mg-biotite, minor to abundant apatite and magnetite, and
333 minor calcite. This type of alteration appears to be closely linked to small syenite and syenite-porphyry intrusions.
334 A well-defined core pyroxene zone is present in some syenite dikes/microdikes with sharp contacts (Fig. 8A).
335 Outside syenite dikes, light grey to light pinkish-grey K-feldspar forms fenite-like zones of pervasive replacement,
336 with a tendency to form fine-grained monomineralic aggregates, evolving into halos of branching K-feldspar
337 veinlets. Some of these K-feldspar zones contain, or are overprinted by, fine- to medium-grained, typically
338 euhedral green to dark-green pyroxene (diopside-hedenbergite), which forms K-feldspar-pyroxene (with minor
339 apatite and/or magnetite) aggregates with an even to patchy distribution of minerals (Fig. 8B-C). Fine-grained
340 diopside-hedenbergite also forms irregular short branching veinlets in monomineralic light grey to light pinkish-
341 grey K-feldspar, locally with apatite and magnetite (Fig. 8D). Apatite (typically 3-7 vol.%, locally up to 10-15
342 vol.%) forms variably-sized crystals and anhedral aggregates (Fig. 8E), intergrown with pyroxene and magnetite.
343 Magnetite is nearly absent in K-feldspar-dominant rocks but reaches 10-20 vol.% in very local intervals with
344 abundant apatite. Encapsulated fine anhydrite crystals are present in apatite. In total, pyroxene-K-feldspar
345 alteration forms the easternmost nearly one-third part of the total potassic alteration halo outcropping on the
346 surface (Fig. 3B) but was encountered by drilling in its other parts, which may represent local domains with no to
347 minor later biotite-K-feldspar overprint. Cu-sulfides (mainly bornite, locally bornite with exsolved chalcopyrite)
348 are rare and occur as small inclusions in magnetite and gangue minerals (Fig. 9A-C).

349 A later potassic alteration assemblage is defined by a broad development of pink to meat-red K-feldspar
350 (orthoclase), which occurs with or without biotite. It starts with gradual pervasive replacement and/or scattered
351 complex-shaped replacement veinlets (Fig. 8F). As the process develops, fine-grained pink K-feldspar replaces
352 broader zones and then evolves into coarser-grained aggregates, typically with the development of dark-brown to
353 greenish-brown biotite (that progressively becomes richer in Fe; Table 3)(Fig. 8G-H). Medium- to coarse-grained
354 (up to 2-3 cm) biotite forms scattered to dense disseminations, complex crystal intergrowths with K-feldspar and
355 magnetite, and small patches (Fig. 8I). Small lens-shaped (<20 cm thick) coarse-grained pegmatite-like K-feldspar-

biotite-magnetite aggregates are locally present (Fig. 8J). Magnetite is ubiquitous (1-5 vol.%) in this assemblage; it is typically finely-disseminated but locally forms larger patchy aggregates. Minor (1-3 vol.%) apatite is present, typically in the form of small euhedral crystals closely associated with biotite (Fig. 8K). Cu-sulfides are most closely associated with biotite (Fig. 8I, L-M), and the biotite-K-feldspar-magnetite-Cu-sulfide assemblage represents the most common type of Cu-Au mineralization at the prospect (Fig. 8J-M); the alteration types containing no biotite are typically barren. On the other hand, the vast majority of biotite-K-feldspar-magnetite alteration, locally with abundant biotite, contains no Cu-sulfides.

Apatite forming large crystals and crystals aggregates in zones of calc-potassic alteration is characterized by slightly elevated Fe, Mn, and Na contents that increase from the inner (core) to outer crystal zones, together with some decrease in Mg, Ba, Sr, and LREE contents (Table 4). Similarly, apatite forming small crystals in the overprinting zones of potassic alteration with intense Cu sulfide mineralization bears higher Fe, Mn, and Na contents, as compared to the larger (earlier) apatite crystals. Overall, apatite is an F-rich variety, with only minor Cl, although Cl contents appear to be slightly higher in the later generation of this mineral (Table 4). Magnetite from calc-potassic and potassic alteration assemblages bears elevated Ti and V (Table 5). As a result, the calc-potassic and potassic alteration assemblages have elevated Ti, V, Zn, Cr (due to admixtures in magnetite), and LREE (due to abundant apatite) contents (Table 6).

Cu-sulfide minerals in zones of biotite-K-feldspar alteration include minor chalcocite, locally intergrown bornite and chalcocite (particularly in coarse-grained, pegmatite-like, K-feldspar-dominant lenses; Fig. 9D), dominant bornite (most typically associated with biotite; Fig. 9E), and chalcopyrite, which forms as exsolution in bornite and as larger aggregates replacing bornite (Fig. 9F-H). Trace to minor hematite replaces bornite and magnetite. Native gold occurs as very fine (typically <0.01 mm, occasionally 1-1.5 mm) disseminations and is closely associated with bornite aggregates and relict bornite in chalcopyrite (Fig 9I-L); there is a positive correlation of Cu and Au grades (Ignatiev et al., 1999). Gold appears to be dispersed in bornite (Table 7); high-finesses native gold enriched in Cu and Pd is also present (Table 8). Sidorov et al. (2017) reported palladium telluride minerals including merenskyite *(Pt, Pd)(Te, Bi)$_2$*, kotulskite *Pd(Te, Bi)*, keithconnite $Pd_{20}Te_7$ and temagamite Pd_3HgTe_3, which are closely associated with bornite-chalcopyrite and chalcocite-bornite-chalcopyrite intergrowths. As a result, the mineralization is characterized by a Cu-Au-PGE geochemical signature (Table 6).

383 The latest potassic substage, comprising sodic-potassic to calcic-sodic-potassic assemblages, is probably
384 transitional to propylitic alteration. It includes fine-grained albite, magnetite, minor biotite, locally calcite, epidote,
385 and trace amphibole. This assemblage is more weakly developed in comparison with earlier alteration, replacing
386 <10 vol.% of the protolith to only form scattered dissemination, patches, and short branching veinlets. Magnetite
387 locally occurs as stockworks of branching veinlets, whilst small (<3 m thick) hydrothermal breccias with a
388 magnetite+albite matrix are observed enclosing clasts that have been subjected to the earlier potassic alteration
389 (Fig. 8N). Chalcopyrite occurs locally in this assemblage but wide intervals with abundant magnetite are barren.
390
391 *7.2 Propylitic alteration*
392 Propylitic alteration occurs in two forms, which correspond to an "inner" and an "outer" propylitic
393 alteration, respectively (cf. Wilson et al., 2003; Corbett, 2017). The "outer" propylitic alteration is represented by
394 fine-grained chlorite to chlorite-amphibole-epidote to chlorite-albite-calcite aggregates that pervasively replace
395 volcanic rocks (Fig. 10A). Pervasive alteration is expressed in selective replacement of mafic minerals by fine-
396 grained chlorite (locally with magnetite and titanite), locally also epidote and amphibole, whereas feldspars are
397 replaced by fine-grained albite±calcite aggregates. Fine-grained magnetite is typical, whereas trace to ubiquitous
398 pyrite and chalcopyrite are present locally. A similar assemblage, with abundant epidote and pyrite, overprints
399 trachytic syenite-porphyry, locally occurring as thin veinlets and breccia matrix (Fig. 10B).
400 The "inner" propylitic alteration occurs within zones of potassic alteration, which are intersected by chlorite-
401 magnetite veinlets, locally accompanied by epidote and/or pyrite (Fig. 10C-D). Similar chlorite-magnetite veinlets
402 intersect trachytic syenite-porphyry and older intrusive rocks. Small intervals of pervasive replacement comprising
403 fine- to medium-grained aggregates of albite, carbonate, epidote (also clinozoisite), magnetite, with minor to trace
404 hematite, chlorite, and amphibole, are also present (Fig. 10E). Quartz is present in trace amounts, typically <2
405 vol.%, but may be absent. Albite-clinozoisite-calcite aggregates containing up to 10-20 vol.% calcite are present in
406 some highly-mineralized intervals that occur in zones of potassic alteration.
407
408 *7.3 Phyllic (carbonate-phyllic) and argillic alteration*

Linear phyllic alteration zones are distinctly associated with the Late Oligocene-Miocene diorite-porphyry dikes and steep-dipping linear fault zones intersecting the prospect area (Fig. 4). These zones overprint earlier alteration types, and result in the replacement of K-feldspar and biotite by a fine-grained quartz-sericite to quartz-sericite-carbonate assemblages. The same structures also locally occupied by subparallel, locally sheeted, carbonate-quartz-sericite veinlets and thin veins (Fig. 10F). Carbonates include both calcite and Fe-Mg varieties (siderite, ankerite, and dolomite). Phyllic alteration assemblages also include pyrite (and locally residual magnetite), possibly hematite, and rare chalcopyrite, sphalerite, and galena. Native gold is occasionally present (up to 13.7 g/t Au; Ignatiev et al., 1999). Nevertheless, the development of phyllic alteration over the earlier Cu-Au mineralized assemblages causes almost entire dilution of Cu and Au grades.

Similarly, argillic alteration occurs in linear zones that are associated with faults intersecting the deposit area. It overprints all earlier alteration types including phyllic alteration. Argillic alteration comprises quartz and kaolinite, and locally trace pyrite. These minerals initially form as fine disseminations, but evolve into porous aggregates, eventually resulting in the complete dilution of Cu and Au mineralization.

8. Rb-Sr isotopic dating

Two samples each of K-feldspar and biotite, and one of whole rock from overlapping calc-potassic and potassic (pyroxene-biotite-K-feldspar) alteration assemblages with Cu-sulfides have been selected for the Rb-Sr isotopic dating.

Rb-Sr analytical data are listed in Table 9. The Rb (121.0–244.3 ppm) and Sr (71.6–2022.3 ppm) contents of the samples vary, yielding $^{87}Rb/^{86}Sr$ values of 0.234 to 10.277. Meanwhile, the $^{87}Sr/^{86}Sr$ values range from 0.703566 to 0.714003. The analytical data yielded a Late Cretaceous isochron age of 73.17±0.54 Ma with an initial $^{87}Sr/^{86}Sr$ ratio of 0.703319±0.000010 (MSWD = 0.15) (Fig. 11).

9. Reconnaissance fluid inclusion study

Due to an almost entire lack of quartz, fluid inclusions at Kirganik were studied in apatite from calc-potassic and potassic alteration assemblages. For this analysis, two generations of apatite are distinguished. The early generation (apatite-1) occurs in calc-potassic alteration assemblages and is associated with pyroxene, locally also

436 magnetite and calcite. It forms aggregates of larger anhedral grains and smaller euhedral crystals. In contrast, the
437 late generation (apatite-2) is represented by smaller euhedral crystals in biotite-magnetite-K-feldspar potassic
438 alteration assemblage with related Cu-sulfide (particularly bornite) mineralization.

439 The early apatite contains a fluid inclusions assemblage (FIA) that comprises silicate melt inclusions and
440 type 1 liquid-gaseous fluid inclusions that occur as isolated individuals. The silicate melt inclusions vary from
441 those containing no gaseous phase to those with variable fractions of silicate melt and gaseous (10-40 vol.%) phase
442 (Fig. 12A-F). Type 1 liquid-gaseous fluid inclusions contain ~35 vol.% gas (Fig. 12G-L). Heating of the silicate
443 melt inclusions, with or without gas phase, indicated no phase changes to the temperature of 650^{o}C (limit of
444 heating). Indeed, the melt inclusions deserve a special study with heating to higher temperatures. Type 1 fluid
445 inclusions, on warming after freezing, exhibit eutectic melting temperatures at -45.5 to -44.0^{o}C indicating a $CaCl_2$-
446 dominant ($CaCl_2$-KCl-NaCl to $CaCl_2$-$MgCl_2$-NaCl) mixture (Crawford, 1981), and the final ice melting at -7.0 to -
447 6.5^{o}C. In the pure NaCl-H_2O system, this would be equivalent to a salinity of ~10 wt.% NaCl-eq. (Bodnar and
448 Vityk, 1994; Table 10). On heating, type 1 inclusions homogenized to liquid at 335-345^{o}C.

449 The late apatite most closely associated with biotite from potassic alteration assemblages contains isolated
450 primary type 2 liquid-gaseous (~20 vol.% gas) inclusions (Fig. 12M-P). On warming after freezing, type 2 fluid
451 inclusions exhibit eutectic melting temperatures at -33.5 to -32.5^{o}C indicating a $MgCl_2$-dominant or $MgCl_2$-KCl-
452 NaCl mixture (Crawford, 1981). Final ice melting occurs at -3.5 to -3.0^{o}C. In the pure NaCl-H_2O system, this
453 would be equivalent to a salinity of about 5 wt.% NaCl-eq. (Bodnar and Vityk, 1994; Table 10). On heating, type
454 2 fluid inclusions homogenized to liquid at 270-280^{o}C.

455

456 **10. Discussion**

457 The Kirganik prospect attracts significant interest because it represents a relatively rare silica-undersaturated
458 subtype of alkalic porphyry Cu-Au systems (Lang et al., 1993, 1995). Such systems/deposits are known in British
459 Columbia, Canada (e.g., Mount Polley, Lorraine, Galore Creek, etc.; Fraser et al., 1995; Logan, 2005; Bissig and
460 Cooke, 2014; Logan and Mihalynuk, 2014; Bath et al., 2014), at the Aldan Shield, Siberia (e.g., Ryabinovoe;
461 Shatova et al., 2019) and in other regions. They are most notably characterized by the silica-deficient causative
462 intrusions and a correspond lack of quartz in hydrothermal alteration assemblages distinguishing them from silica-

463 saturated alkalic porphyry Cu-Au systems (e.g., Barr et al., 1976; Lang et al., 1993, 1995; Bissig and Cooke, 2014;
464 Misco et al., 2014; Byrne and Tosdal, 2014; Devine et al., 2014; Pass et al., 2014). Other distinct signatures typical
465 of the entire alkalic porphyry Cu-Au deposit type include the limited development to lack of the most acidic
466 (argillic, etc.) alteration types (e.g., Holliday and Cooke, 2007), stronger development of calcic (calc-potassic,
467 calcic-sodic) assemblages, and greater role of magmatic-hydrothermal Ca-rich fluids (Sillitoe, 2010). As a result,
468 the Kirganik prospect complements the diversity of porphyry Cu-Au deposits in the Northwest Pacific, where both
469 calc-alkaline (e.g., Malmyzh; Soloviev et al., 2019b) and silica-saturated alkalic (e.g., Peschanka, Lazurnoe;
470 Muller and Groves, 2019; Soloviev et al., 2019a) porphyry Cu-Au deposits are present.
471
472 *10.1 Tectonic setting and magma sources*
473 The Kirganik prospect was formed in a Late Cretaceous island arc that was developed in response to the
474 westward subduction of the Pacific plate (e.g., Yakubchuk, 2009). Consistently, the most pronounceable
475 geochemical characteristics of the shoshonitic rocks at Kirganik (Table 2; Fig. 6G), such as Ta, Nb, and Ti
476 depletion and Pb enrichment, show a distinct subduction-related, island arc rock affinity (cf. Kepezhinskas, 1994;
477 Pearce and Peate, 1995; Dalslaen et al., 2020). The Ta-Nb-Ti depletion is explained by the retaining of these
478 elements in refractory mineral phases (such as rutile, etc.) under a low degree (~1-3 vol.%) of partial melting of a
479 metasomatized K-rich lithospheric mantle, particularly such as amphibole-spinel peridotite, or spinel lherzolite
480 (e.g., Meen, 1987; Pearce and Peate, 1995; Fig 13A-B). Together with high K contents, the rocks are characterized
481 by high P, Ba, and Sr contents that can also be related to metasomatic enrichment of the lithospheric mantle
482 resulting in the formation of phlogopite, spinel, apatite, and/or amphibole (e.g., Folley and Peccerillo, 1992). On
483 the other hand, the rocks are characterized by the very low LREE (<20 ppm La, <30 ppm Ce), low to slightly
484 elevated LILE (e.g., typically <100 ppm Rb), and low HFSE (<0.90 wt.% TiO_2, <105 ppm Zr, <5 ppm Nb)
485 contents (Table 2). The low LREE contents could be explained by early apatite crystallization, as apatite is a very
486 early liquidus phase in mafic melts, but the high P, Ba and Sr suggest that later apatite was present in the more
487 evolved rocks. Alternatively, these signatures may represent a weaker metasomatic alteration of the lithospheric
488 mantle during an island arc development (e.g., Dalslaen et al., 2020), more specifically in the absence of essential
489 LILE supply from the subducting slab and possibly under a dominant fluid-derived (vs. slab-derived; Fig. 13C)

490 metasomatic process (cf. Hanyu et al., 2006). The latter may explain the lack, to weak increase of LILE, LREE and
491 HFSE concentration of lithospheric (possibly depleted) mantle material (e.g., Muller and Groves, 2019). The
492 magma source enrichment continued during the magma generation (Fig. 13D), thus contributing to the
493 replenishment of magmatic reservoir to form younger intrusive phases (cf. Moritz et al., 2016). Koloskov et al.
494 (1999, 2009) suggested the emplacement of the Late Cretaceous-Paleogene potassic rocks in Central Kamchatka
495 during the initial rifting in a mature island arc, with possible shoshonitic-lamproitic transition. Overall, the island
496 arc setting of the Kirganik prospect corresponds to that of alkalic porphyry Cu-Au deposits with a low Mo content
497 (Richards, 2011; Muller and Groves, 2019), the latter possibly due to a weaker metasomatic enrichment of the
498 lithospheric mantle and/or lesser amount of the ancient continental crustal material involved (e.g., Pettke et al.,
499 2010).

500 In the broader Central Kamchatka region, isotopic K-Ar ages of igneous rocks similar to those at Kirganik
501 was defined at 86 to 52 Ma, whereas U-Pb zircon age were 70.4±0.7 Ma to 63.0±0.6 Ma (Slyadnev et al., 2006;
502 Hourigan et al., 2004). A wide span of the K-Ar isotopic ages (from 37.5 to 75 Ma) obtained in the 1960s was also
503 reported for the "biotite-K-feldspar-altered volcanic rocks" at the Kirganik prospect (e.g., Flerov and Seliverstov,
504 2008). Our first isotopic Rb-Sr age data (73.17±0.54 Ma) obtained for mineralized potassic alteration assemblages
505 at Kirganik are in agreement with a Late Cretaceous (Campanian to Maastrichtian-Campanian) age, thus
506 supporting their links to potassic igneous rocks emplaced during island arc development. However, the younger
507 members of the long-lasting succession of potassic igneous rocks can also be present at Kirganik, as evidenced by
508 the presence of trachytic syenite-porphyry crosscutting the main potassic alteration assemblages.
509

510 *10.2 Magmatic-hydrothermal evolution*

511 The data suggest a complex, possibly cyclic magma differentiation that likely involved fractionation in
512 peripheral, low-pressure magma chambers, as indicated by the close association of volcanic, subvolcanic and
513 plutonic rocks, common porphyry and flow textures, presence of quenched melt inclusions and other signatures.
514 This rock sequence reflects the crystallization differentiation of a silica-undersaturated magma, which tends to
515 produce feldspathoidal-alkali-feldspar rocks (e.g., Schairer and Yoder, 1960; Bonin and Giret, 1984). A negative
516 correlation between Dy/Yb ratios and increasing SiO_2 contents indicates an amphibole fractionation in a deep

(lower crustal ?) magma chamber (Fig. 13E; Davidson et al., 2007; Moritz et al., 2016). In contrast, the lack or scarcity of amphibole phenocrysts in the rocks, even in their most fractionated varieties, indicates that the fractionation of accessory minerals (apatite, magnetite, etc.), clinopyroxene and possibly biotite appears to be the main magma differentiation process in peripheral magma chambers (Fig. 13F). The role of plagioclase fractionation was also relatively minor resulting in the lack of Eu anomalies (Fig. 6G), although the role of K-feldspar fractionation was more pronounced (Fig. 13F). The presence of biotite (vs. amphibole) may be indicative of the water saturation in a higher aK^+ and/or fO_2 environment. Alternatively, the primitive clinopyroxene-dominant composition and crystallization of biotite occurring in the K-enriched alkaline arc series may indicate a lower water saturation (e.g., Bucholz et al., 2014).

Magnetite fractionation was part of the dominant accessory mineral fractionation process and is evidenced by the abundance of magmatic magnetite in all igneous rocks at Kirganik. Separation of magnetite in hydrous, oxidized arc magmas facilitates H_2O saturation and further massive exsolution of magmatic-hydrothermal aqueous phase (e.g., Knipping et al., 2015b). Separation of immiscible iron oxide to hydrous Fe-Ca-P melt(s), with the two-liquid field expanding under increasing aH_2O and fO_2 thus allowing the Fe-Ca-P melt to separate easily from host silicate magma, was also possible (Hou et al., 2018). This highlights the importance of the pyroxene-K-feldspar-apatite-magnetite rocks at Kirganik, with minor calcite and Mg-biotite, that appear to be closely associated with syenite to syenite-porphyry and exhibit "mixed" igneous to hydrothermal-metasomatic signatures. Notably Mungall et al. (2018) reported immiscible shoshonitic and Fe-P-oxide melts, whereas Knipping et al. (2015a, b) suggested an early formation of a clinopyroxene-magnetite-apatite assemblage from an immiscible Fe-Ca-P melt, with its further development from a hydrothermal fluid. The segregation of magnetite (to Fe-Ca-P) melt occurring at ~60 wt.% SiO_2 could be triggering the segregation of Cu-sulfide melt due to abrupt change of the oxidation state and conversion of most of the sulfur originally dissolved in the magma as sulfate, with the Cu-rich sulfide phase represented by bornite sequestering gold (cf. Jenner et al., 2010). Sun et al. (2015) also emphasized that sulfide saturation in an oxidized magma occurs and the metals are partitioned into coexisting magmatic-hydrothermal fluids following sulfate reduction accompanying magnetite crystallization.

Protracted stability of Cu-sulfide melts at temperatures as low as 500°C, rather than a rapid Cu and sulfur transition into an aqueous magmatic-hydrothermal fluid, can also be envisioned (e.g., Halter et al., 2005; Simpson,

2014; Mernagh and Mavrogenes, 2019; Govindarao et al., 2020; Huang et al., 2020). Holwell and Blanks (2021) reported the development of Cu-Au-Te (-Ni-PGE) sulfide blebs that are texturally associated with calcite in mineralization related to mafic alkaline rocks and formed from the cooling of a Cu-dominant sulfide liquid. This could be facilitated by both a low water and sulfur content, the latter being typical of silica-undersaturated porphyry Cu-Au deposits and expressed in the dominant low-sulfur Cu-sulfides and scarcity of pyrite (cf. Simon et al., 2006). The coexistence of a Cu-sulfide melt with the fluid causing potassic alteration would further explain the widespread massive Cu-sulfide "pods" and blebs at Kirganik. The presence of Cu-sulfide droplets in magnetite and gangue minerals (Fig. 9A-C) supports this possibility. Progressing magma differentiation and water saturation results in the metal/sulfur partitioning into a coexisting magmatic-hydrothermal fluid (e.g., Burnham, 1997; Student and Bodnar, 2004; Audetat et al., 2008; Wilkinson, 2013; Sun et al., 2015), with further transition toward the "more typical" post-magmatic potassic alteration assemblages dominated by biotite and K-feldspar, with minor magnetite and most intense deposition of Cu-sulfides. The staged fluid exsolution from crystallizing magma would follow the formation of residual magma chambers in a cooling pluton (Fig. 15).

10.3 Fluid inclusion data interpretation

The gas bubble homogenization temperatures measured for type 1 and 2 fluid inclusions in apatite from the calc-potassic and potassic alteration assemblages (335-345^{o}C and 270-280^{o}C, respectively) appear to be too low as compared to the generally high-temperature (~450-550^{o}C) conditions of sericite-free calc-potassic and potassic alteration known at many porphyry Cu deposits (for example, see review in Tsuruoka, 2017). Attributing this difference to the respective pressure correction, trapping pressure can be estimated for type 1 and 2 fluid inclusions using the data on isochores for H_2O-NaCl solution of salinities and homogenization temperatures corresponding to those defined in this study (i.e., 5 and 10 wt.% NaCl-eq., and 275^{o}C and 340^{o}C; Fig. 14). Applying the high (~450-550^{o}C) trapping temperatures, these estimates yield a high pressure of ~2.2 kbar and ~2.1 kbar, respectively. Applying lower trapping temperatures (e.g., 400° to 420°C) yields a lower pressure; however, these lower temperatures (even considering a fluxing role of volatiles in residual magmas) would be rather inconsistent with the transitional magmatic-hydrothermal signatures of the calc-potassic alteration assemblages at Kirganik. Nevertheless, these lower entrapment temperatures may be more plausible for the later, most mineralized potassic

alteration assemblages, and the corresponding trapping pressures can be estimated in the range of ~1.5 to ~1.8 kbar (Fig. 14). The fluid entrapment temperatures >400°C (i.e., at the temperatures higher than those of the brittle-ductile transition; cf. Fournier, 1999), would be supported by the lack of sulfide veinlets but, in contrast, by replacement-style mineralization related to potassic alteration at Kirganik.

The respective depth estimates would be strongly dependent on the lithostatic pressure gradient that can range from 3.3 km/100 Mpa (1 kbar) (e.g., Hagemann and Brown, 1996) to 3.8 km/100 Mpa (Shepherd et al., 1985) to 4 km/100 Mpa (Fournier, 1999). Consistently, applying the lowest lithostatic pressure gradient for the pressure of ~2.1-2.2 kbar yields a depth of ~7 km, and that for the pressure of ~1.5-1.8 kbar – a depth of 5-6 km. In contrast, applying the highest lithostatic pressure gradient for the same pressures yields a depth of ~9 km to ~6 km. Thus, although the lower P-T (400-420°C and ~1.5 kbar) and depth (~5 km) estimates are similar to those characterizing the main Cu mineralization stage in many porphyry Cu deposits (e.g., Kouzmanov and Pokrovski, 2012, and references therein), the others suggest rather a deeper, possibly root-level of the porphyry system (cf. Sillitoe, 1973, 2010; Seedorff et al., 2008). Also, a significant pressure drop (for >0.5 kbar) is unlikely during a short timespan between calc-potassic and potassic alteration. Nevertheless, the lack of carbonic phases in the fluid inclusions is consistent with mineralization occurring at shallower (~5 km) depths, where CO_2 is immiscible with aqueous fluids at lithostatic pressures (e.g., Baker, 2002; Kouzmanov and Pokrovski, 2012). The formation of mineralization and alteration at a depth of ~5 km or slightly greater is consistent with the prospect location within the ~3 km thick Irunei suite overlain by the ~3km thick Kirganik suite (Ignatiev et al., 1999), resulting in a cumulative ~6 km thickness of the host volcanic rocks. The latter would further correspond to the weak porphyry appearance of most of igneous rocks at Kirganik. Porphyroblastic and branching K-feldspar "injections" associated with syenite also represent a deep porphyry-level signature, and so are pegmatitic biotite-K-feldspar-magnetite veins. The sharply porphyritic trachytic syenite-porphyry postdating the main potassic alteration and related mineralization event may indicate a different depth of emplacement of these later rocks.

The fluid inclusion data at Kirganik demonstrate a lack of hypersaline brine, multi-solid (with halite, sylvite, etc.) fluid inclusions, incorporating variable amounts of gas and liquid, that would either occur solely or coexist with low-salinity (gaseous, gaseous-liquid) fluid inclusions, the latter indicating fluid boiling (e.g., Roedder, 1984; Bodnar et al., 2014; Becker et al., 2019). Instead, the fluid inclusion assemblages at Kirganik contain type 1 and

598 type 2 liquid-gaseous fluid inclusions with no chloride solids that either coexist with silicate melt inclusions or
599 occur alone. Silicate melt inclusions coexisting with fluid inclusions were noted in quartz from hydrothermal veins
600 at many other porphyry Cu-Au deposits and are interpreted to indicate a magmatic-hydrothermal transition (Halter
601 et al., 2005; Harris et al., 2003, 2004; Stefanova et al., 2014; Mernagh and Mavrogenes, 2019). Furthermore, the
602 low-salinity (~5 to 10 wt.% NaCl-eq.) type 1 and type 2 fluid inclusions can represent the high temperature single-
603 phase supercritical fluid (Sillitoe, 2010; cf. Becker et al., 2019) that exsolves from a cooling pluton at the early
604 stages of its crystallization. As noted by Sillitoe (2010), porphyry Cu mineralization in the deeply formed potassic
605 alteration zones took place directly from a single-phase, relatively low salinity (2-10 wt.% NaCl-eq.) aqueous fluid.
606 As emphasized by Becker et al. (2019), these conditions correspond to the early stages of pluton crystallization, on
607 or near the water-saturated solidus, when silicate melt, crystals, and magmatic fluid coexist and can be entrapped
608 by crystallizing minerals. Only at shallower levels, the fluid enters the two-phase immiscibility region, with
609 coexisting hypersaline liquid (brine) and vapor. Notably, even the low salinity fluid was able to transport and
610 deposit substantial amounts of Cu, Au, and other metals (e.g., Audetat et al., 2008; Bekker et al., 2019).
611 The fluid inclusion composition, particularly their high Ca content, inferred from this study is consistent
612 with the common greater role of magmatic-hydrothermal Ca-rich fluids at alkalic porphyry Cu-Au deposits
613 (Sillitoe, 2010). At Kirganik, this is further aligned with the broad development of calc-potassic alteration
614 assemblages that, among other Ca minerals (e.g., apatite, calcite), include hydrothermal pyroxene. Pyroxene and/or
615 garnet are abundant in calc-potassic alteration assemblages at many alkalic porphyry Cu-Au deposits (e.g.,
616 Chamberlain et al., 2007; Wolfe and Cooke, 2011; Misco et al., 2014; Devine et al., 2014; Bouzari et al., 2016).
617
618 *10.4 Possible geological setting models*
619 Several geological models can be invoked to explain the present geometry of the Kirganik prospect (Fig.
620 16). The simplest model would involve flat-lying mineralized zones within tensional structures above a contracting
621 cupola-shaped pluton at depths in excess of the currently deepest drilling (i.e., >500 m; Fig. 16A). However, this
622 would require a different fluid inclusion assemblage in the hydrothermal alteration minerals (cf. Becker et al.,
623 2019). Furthermore, the lack of phyllic/argillic alteration associated with the porphyry system is inconsistent with
624 its shallow erosion, and the absence of mineralization, other than a few narrow intervals, for ~500 m below the

main zone. An alternative might involve mineralization controlled by flat-lying thrust-like structures, with the metalliferous fluid source located beyond the prospect area (Fig. 16B). Although thrust-faults are found in the broader region (e.g., Kovalenko, 2010), none were formed during the island arc stage of tectonic development.

A third alternative, and the most consistent with observations, involves a rapid tilting of the mineralized system by up to 90º soon after its formation. In this model, a subvertical package of vertically extensive, but, narrow intrusive apophyses and alternating zones of calc-potassic and potassic alteration, with associated subvertical lenticular zones of mineralization, has been tilted and largely eroded, so that a significant (>1.5 km) section of the column is now horizontal and exposed at the surface. Although further work is required to demonstrate possible tectonic fabrics supporting such a tilt, this model would resolve the controversy of the presently steeply dipping volcanic-sedimentary sequence, by re-establishing its pre-tilt, initial shallow bedding. This model would also be in agreement with the presence of the high-pressure, low-salinity liquid-gaseous fluid inclusions, some of which coexist with silicate melt inclusions, as the deep porphyry level was exhumed after tilting. The latter explains the root-level signatures of hydrothermal alteration and mineralization at Kirganik. A greatly extended subvertical setting of narrow, finger-like intrusions and mineralized zones occurs at many shoshonite-related porphyry Cu-Au deposits (e.g., Wolfe and Cooke, 2011; Pacey et al., 2019), and significant post-mineral tilt is recognized at some of them (Seedorff et al., 2008; Misco et al., 2014; Devine et al., 2014). However, younger (crosscutting) and apparently subvertical subvolcanic intrusions at Kirganik suggest that potassic magmatic activity in the prospect area could be continuing after the tilt.

10.5 Geochemical signatures of mineralized rocks

At least two distinct geochemical assemblages can be distinguished in mineralized rocks at Kirganik (Table 6). First, magnetite-rich intervals are characterized by high Ti, V, Zn, P, Ca, Mn contents, together with elevated Cu and Au. This corresponds to the high contents of magnetite and apatite, the main minerals concentrating these elements (Tables 4, 5), and to the trace to minor Cu-Au mineralization. Particularly high Ti contents are inconsistent with the low-Ti geochemical signature of the parental shoshonitic igneous rocks studied, although higher-Ti intrusive varieties can be present elsewhere at the prospect; more realistic, however, is to assume that Ti (an immobile element) was retained from the higher-Ti volcanic rocks now essentially to completely altered and

652 replaced by hydrothermal assemblages. Nevertheless, high Ti and V contents, as well as higher Al and Mn, are
653 usually attributed to magmatic, rather than to hydrothermal, generations of magnetite and biotite that were
654 crystallized under higher temperatures (e.g., Nadoll et al., 2014). Overall, this may indicate the respective
655 transitions to the magmatic Fe-Ti-oxide, V-rich mineralization, thus expanding the compositional variability of
656 alkalic porphyry Cu-Au systems (e.g., Beaudoin and Dupuis, 2009; Nadoll et al., 2014; Fig. 17). Not all
657 generations of magnetite, however, appear to be enriched in Ti, V and associated elements, with these contents
658 decreasing toward the lower temperature varieties (Table 5). An elevated Mn content in apatite corresponds to that
659 typical for alkalic porphyry Cu-Au deposits (Mao et al., 2016).

660 Second, porphyry Cu-Au mineralization at Kirganik is characterized by a distinct enrichment in PGE,
661 particularly Pd and, to lesser extent, Pt (Table 6; Ignatiev et al., 1999; Sidorov et al., 2017). Although elevated
662 PGE contents are common in many porphyry Cu-Au deposits and particularly in their alkalic, shoshonite-related
663 members (e.g., Thompson et al., 2001; LeFort et al., 2011; Bissig and Cooke, 2014), the particular abundance of
664 PGE mineralization at Kirganik constitutes a remarkable geochemical signature that possibly points toward a
665 greater magmatic component in mineralizing fluids.

666

667 *10.6 Shoshonite-related porphyry Cu-Au versus IOCG-style deposit affinity*

668 There are a number of characteristics at Kirganik, which are reminiscent of those of the Iron Oxide Copper-
669 Gold (IOCG) deposit family, together with the general Cu-Au profile of mineralization. These include (1)
670 relationships to alkaline potassic mafic magmas, (2) local abundance of magnetite in zones of hydrothermal
671 alteration, (3) local abundance of apatite and its association with magnetite, (4 dominant magnetite-bornite
672 association, abundance of low-S sulfides (bornite, chalcopyrite, and chalcocite), and scarcity of pyrite (cf.
673 Corriveau and Mumin, 2010; Groves et al., 2010; Barton, 2014). Pyroxene-apatite-magnetite rocks, which are
674 present at Kirganik, also occur at some IOCG and related "precursor" iron-oxide deposits (e.g., Williams et al.,
675 2005; Knipping et al., 2015b).

676 The similarities of alkalic porphyry Cu-Au deposits and the magmatic-hydrothermal IOCG-family deposits
677 were examined by Richards and Mumin (2013a,b). Richards et al. (2017) further emphasized the back-arc settings
678 of the silica-undersaturated alkalic porphyry Cu-Au deposits, similar to the settings of IOCG deposits but

679 contrasting to main arc settings of silica-saturated porphyry Cu-Au deposits, and the generation of magmas from
680 upwelling asthenosphere distal to a subduction zone, the latter likely facilitating a greater involvement of more
681 primitive, alkaline magmas. In this respect, the affinity of the alkalic porphyry and magmatic-hydrothermal IOCG
682 deposits reflects their global links to shoshonitic magmatism (e.g., Groves et al., 2010; Soloviev, 2014; Muller and
683 Groves, 2019).
684

685 ## 11. Conclusions

686 The Kirganik prospect represents a silica-undersaturated, shoshonite-related (alkalic) porphyry Cu-Au
687 system occurring in the Late Cretaceous island arc of Central Kamchatka. It is associated with a volcanic-plutonic
688 suite that comprises potassic alkaline rocks varying from monzogabbro- and monzodiorite-porphyry to monzonite-
689 and syenite-porphyry, and then to another (compositionally overlapping) cycle of magma emplacement comprising
690 trachytic syenite-porphyry and possibly other, more differentiated intrusive phases. The rocks exhibit a subduction-
691 related, island arc rock affinity, with the magma generation involving low degree (~1-3 vol.%) partial melting of
692 metasomatized, K-rich lithospheric mantle, followed by amphibole fractionation in a deep, probably lower crustal,
693 magma chamber, with subsequent fractionation of accessory minerals, clinopyroxene and possibly biotite in
694 shallower magma chambers. The staged fluid exsolution from crystallizing magma could reflect the development
695 and discharge of subsequent residual magma chambers in a cooling pluton, with their gradual enrichment in water
696 and fluxing components (K, P, etc.) and then a greater enrichment in water and metals (Cu, Au), as magma
697 differentiation progressed.

698 The prospect comprises K-feldspar-pyroxene-apatite-Ti-magnetite rocks closely related to syenite intrusions,
699 which evolve into zones of pyroxene-K-feldspar-apatite-Ti-magnetite (calc-potassic) alteration. This alteration
700 assemblage is overprinted by wider, replacement-style zones of biotite-K-feldspar-magnetite (potassic) alteration,
701 some of which contain abundant Cu-sulfides (mostly bornite and chalcopyrite, with minor chalcocite). Subsequent
702 albite-magnetite-calcite-epidote (sodic-potassic to calcic-sodic-potassic) and chlorite-magnetite-epidote±pyrite
703 (propylitic) alteration have much weaker development. Native gold is closely associated with bornite and, to a
704 lesser degree, with chalcopyrite. The prospect is characterized by a strong enrichment in PGE (particularly Pd),

705 together with a strong Ti-V geochemical signature of hydrothermal magnetite. This expands compositional
706 variability of the alkalic porphyry Cu-Au systems.

707 Apatite from calc-potassic (pyroxene-K-feldspar) and potassic (biotite-K-feldspar) alteration at Kirganik
708 contains low salinity (5-10 wt.% NaCl-eq.) liquid-gaseous fluid inclusions. This indicates a homogenous, low-
709 salinity, supercritical aqueous fluid directly exsolving from cooling and degassing pluton, and differs from the fluid
710 inclusion assemblages that are common at many porphyry Cu-Au deposits comprising chloride brine (with or
711 without coexisting gaseous) inclusions. Under inferred high temperatures of calc-potassic and potassic alteration
712 (450-550 to 400-420^{o}C) and significant (2.1-2.2 to 1.5-1.8 kbar) pressure, this suggests a deep (>5 km ?), possibly
713 root-level of a larger, shallower, since eroded, porphyry Cu-Au system. The low salinity fluid was able to transport
714 substantial amounts of Cu, Au, and other metals.

715 The models considering various structural settings of mineralized zones may explain some features of the
716 spatial distribution of causative intrusions, related hydrothermal alteration and Cu-Au mineralization at Kirganik,
717 and may provide vectors toward the better-preserved parts of the respective modeled magmatic-hydrothermal
718 systems. A model considering a sharp (up to 90^{o}) post-mineral tilt of the initially subvertical setting appears to be
719 most favorable to explain the prospect features, particularly the deep-level, root-like appearance of hydrothermal
720 alteration and mineralization, and their occurrence in relation to flat-lying, sill-like causative intrusions.

721 The prospect exhibits some signatures, which are common for both alkalic (silica-undersaturated)
722 shoshonite-related porphyry Cu-Au deposits and the IOCG-family deposits. These affinities are fundamentally
723 determined by their global links to shoshonitic magmatism.

724

725 **Acknowledgments**

726 This paper represents part of the authors' work on research and assessment of porphyry Cu-Au deposits in
727 eastern Russia. Andrei Montin, Ivan Trunin, and Alexander Efimov participated in the fieldwork. Elena Kovalchuk
728 (IGEM RAS) performed electronic microprobe analysis. The authors are grateful to these colleagues as well as to
729 Ken Tainton, Jason Campbell, Stephen McIntosh, Sergei Diakov, George Steele, Nick Hawkes, Evgeny Ignatiev,
730 Evgeny Sidorov and others for fruitful and inspiring discussions. Tom Bowens (IG Copper) is thanked for allowing
731 permission to publish the data. The work was financially supported by the Project no. 075-15-2020-802 of the

Russian Ministry of Education and Science, Scientific Program of IGEM RAS, and by the Contract no. 049-00013-20-00 of TsNIGRI. Editorial reviews by Franco Pirajno, Peter Lightfoot and two anonymous reviewers significantly improved the paper.

REFERENCES

Atkinson A.B., 2002. A model for the PTX properties of H_2O-NaCl. M.Sc.Thesis, Virginia Tech. Institute and State University, 126 pp.

Audetat A., Pettke T., Heinrich C.A., Bodnar R.J., 2008. The composition of magmatic-hydrothermal fluids in barren and mineralized intrusions. Econ. Geology 103, 877-908

Barr, D.A, Fox, P.E., Northcote, K.E., Preto, V.A., 1976. The alkaline suite porphyry deposits; a summary. Canadian Institute of Mining and Metallurgy, Special Volume 15, p. 359–367

Barton, M.D., 2014. Iron oxide (–Cu–Au–REE–P–Ag–U–Co) systems. Treatise on Geochemistry. 2nd edition, pp. 515–541

Bath A. B., Cooke D. R., Friedman R. M., Faure K., Kamenetsky V. S., Tosdal R. M., Berry R. F., 2014. Mineralization, U-Pb geochronology, and stable isotope geochemistry of the Lower Main Zone of the Lorraine deposit, North-Central British Columbia: A replacement-style alkalic Cu-Au porphyry. Econ. Geology 109, 979-1004

Beaudoin, G., Dupuis, C., 2009. Iron-oxide trace element fingerprinting of mineral deposit types. In: Corriveau, L., Mumin, H. (eds.), Exploring for Iron Oxide Copper–Gold Deposits: Canada and Global Analogues, Short Course Volume. Geol. Assoc. Canada Annual Meeting, pp. 107–121

Baker T., 2002. Emplacement depth and carbon dioxide-rich fluid inclusions in intrusion-related gold deposits. Econ. Geol. 97, 1111–1117

Becker S.P., Bodnar R.J., Reynolds T.J., 2019. Temporal and spatial variations in characteristics of fluid inclusions in epizonal magmatic-hydrothermal systems: Applications in exploration for porphyry copper deposits. J. Geochem. Exploration 204, 240-255

Becker S.P., Fall A., Bodnar R.J., 2008. Synthetic fluid inclusions. XVII. PVTX properties of high-salinity H_2O-NaCl solutions (>30 wt.% NaCl): applications to fluid inclusions that homogenize by halite disappearance from porphyry copper and other hydrothermal ore deposits. Econ. Geol. 103, 539-544

Bissig T., Cooke D.R., 2014. Introduction to the special issue devoted to alkalic porphyry Cu-Au and epithermal Au deposits. Econ. Geology 109, 819-825

760 Bodnar R.J., Burnham C.W., Sterner S.M., 1985. Synthetic fluid inclusions in natural quartz. III. Determination of phase
761 equilibrium properties in the system H_2O-NaCl to 1000°C and 1500 bars. Geochim. Cosmochim. Acta 49, 1861–1873
762 Bodnar R.J., Lecumberri-Sanchez P., Mancada D., Steele-MacInnis M., 2014. Fluid inclusions in hydrothermal ore deposits.
763 In: Holland H.D., Turekian K.K. (eds.), Treatise on Geochemistry, 2nd ed., v. 13. Elsevier, Oxford, pp.119-142
764 Bodnar R.J., Vityk M.O., 1994. Interpretation of microthermometric data for H_2O-NaCl fluid inclusions. In: De Vivo B.,
765 Frezzotti M.L. (Eds) Fluid inclusions in minerals, methods and applications. Blacksburg, Virginia Tech, pp. 117-130
766 Bonin B., Giret A., 1984. The plutonic alkaline series: the problem of their origin and differentiation, the role of their
767 mineralogical assemblages. Physics of the Earth and Planetary Interiors 35, 212-221
768 Bouzari F., Hart C.J.R., Bissig T., Barker S., 2016. Hydrothermal alteration revealed by apatite luminescence and chemistry: A
769 potential indicator mineral for exploring covered porphyry copper deposits. Econ. Geology 111, 1397-1410
770 Bucholz C.E., Jagoutz O., Schmidt M.W., Sambuu O., 2014. Fractional crystallization of high-K arc magmas: biotite- versus
771 amphibole-dominated fractionation series in the Dariv Igneous Complex, Western Mongolia. Contrib. Mineral. Petrol.
772 168(5):1072, 1-28
773 Burnham, C.W., 1997. Magmas and hydrothermal fluids. In: Barnes, H.L. (ed.), Geochemistry of Hydrothermal Ore Deposits.
774 Wiley and Sons, New York, pp. 63-123
775 Byrne, K., Tosdal, R.M., 2014. Genesis of the Late Triassic Southwest zone breccia-hosted alkalic porphyry Cu-Au deposit,
776 Galore Creek, British Columbia, Canada. Econ. Geology 109, 915-938
777 Chamberlain C.M., Jackson M., Jago C.P., Pass H.E., Simpson K.A., Cooke D.R., Tosdal R.M., 2007. Toward an integrated
778 model for alkalic porphyry copper deposits in British Columbia. In: Geological Fieldwork 2006, British Columbia
779 Ministry of Energy, Mines and Petroleum Resources, paper 2007-1, p.259-273
780 Chappell B.W., White A.J.R., 1992. I- and S-type granites in the Lachlan Fold Belt. Trans. Royal Soc. Edinburgh, Earth
781 Sciences 83, 1-26
782 Cooke D.R., Wilson A.J., House M.J., Wolfe R.C., Walshe J.L., Lickfold V., Crawford A.J., 2007. Alkalic porphyry Au-Cu
783 and associated mineral deposits of the Ordovician to Early Silurian Macquarie Arc, New South Wales. Austr. J. Earth
784 Sciences 54, 445-463
785 Corbett. G.J., 2017. Epithermal Au-Ag and porphyry Cu-Au exploration. Short Course Manual, Sept. 2017 edition.
786 www.corbettgeology.com
787 Corriveau L., Mumin H. (eds.), 2010. Exploring for iron oxide copper-gold deposits: Canada and global analogues. Geological
788 Association of Canada. Short Course Notes 20, University of Newfoundland, St.John's. 185 p.

789 Crawford M.L., 1981. Phase equilibria in aqueous fluid inclusions. In: Hollister L.S., Crawford M.L. (eds.), Fluid inclusions:
790 Application to Petrology. Min Assoc Canada Short Course Handbook, Calgary 6, pp.75-100
791 Dalslåen B.H., Gasser D., Grenne T., Augland L.E., Corfu F., 2020. Ordovician shoshonitic to ultrapotassic volcanism in the
792 central Norwegian Caledonides: The result of sediment subduction, mantle metasomatism and mantle partial melting.
793 Lithos 356-357, 105372
794 Davidson J., Turner S., Handley H., Macpherson C., Dosseto A., 2007. Amphibole "sponge" in arc crust? Geology 35, 787–
795 790
796 Development Strategy for Mining and Processing of Mineral Resources in Kamchatka, 2017. Annual Report, KamchatNedra,
797 Russian Ministry of Natural Resources. (in Russian) https://gold.1prime.ru/reviews/20170418/196044.html
798 Devine F.A.M., Chamberlain C.M., Davies A.G.S., Friedman R., Baxter P., 2014. Geology and district-scale setting of tilted
799 alkalic porphyry Cu-Au mineralization at the Lorraine deposit, British Columbia. Econ. Geology 109, 939–977
800 Fedorov P.I., Dubik F.Y., 1990. The Late Cretaceous shoshonitic assemblage of Central Kamchatka. Internat. Geology Rev.
801 10, 972-980
802 Fedorov P.I., Shantzer A.E., Flerov G.B., Koloskov A.V., Ananiev V.V., 2013. Relationships between the Kirganik and
803 Kitilgin high-potassic volcanic-plutonic complexes in Kamchatka. Proc. KRAUS, Earth Sciences 21(1), 44-52 (in
804 Russian)
805 Flerov G.B., Koloskov A.V., 1976. Alkaline Basaltic Magmatism of the Central Kamchatka. Moscow, Nauka Publishing. 147
806 p. (in Russian)
807 Flerov G.B., Fedorov P.I., Churikova T.G., 2001. Geochemistry of Late Cretaceous–Paleogene potassic rocks of the early
808 evolutionary stage in the Kamchatka island arc. Petrology 9 (2), 161-178
809 Flerov G.B., Seliverstov V.A., 2008. Cretaceous–Paleogene magmatism of the Sredinnyi Range of Kamchatka: magma
810 sources. Volcanol. Seismol. 2, 71–82
811 Foley S.F., Peccerillo A., 1992. Potassic and ultrapotassic magmas and their origin. Lithos 28, 181-185
812 Fournier R.O., 1999. Hydrothermal process related to movement of fluid from plastic into brittle rock in the magmatic-
813 epithermal environment. Econ. Geol. 94, 1193-1212
814 Fraser T.M., Stanley C.R., Nikic Z.T., Pesalj R., Gorc D., 1995. The Mount Polley alkalic porphyry copper-gold deposit,
815 south-central British Columbia. In: Schroeter T.G. (ed.), Porphyry deposits of the northwestern Cordillera of North
816 America. Canadian Institute of Mining, Metallurgy and Petroleum Special Volume 46, p. 609-622
817 Goldstein R.H., Reynolds T.J., 1994. Systematics of fluid inclusions in diagenetic minerals. Soc Sediment Geol Short Course
818 31, 199 p.

819 Goryachev, N.A., Pirajno, F., 2014. Gold deposits and gold metallogeny of Far East Russia. Ore Geology Rev. 59, 123-151
820 Goryachev, N.A., Volkov, A.V., Sidorov, A.A., Gamyanin, G.N., Savva, N.E., Okrugin, V.M., 2010. The epithermal Au–Ag-
821 mineralization in volcanic belts of northeast Asia. Lithosphere 3, 36–50 (in Russian).
822 Govindarao B., Lochan Pruseth K., Mishra B., 2020. Experimentally produced Cu-Pb-Ag-Sb-S melts at 500 °C: implications
823 to partial melting of massive sulfide ores. Ore Geology Rev. 121, paper 103560, 1-9
824 Groves D.I., Bierlein F.P., Meinert L.D., Hitzman M.W., 2010. Iron oxide copper gold (IOCG) deposits through Earth history:
825 implications for origin, lithospheric setting, and distinction from other epigenetic iron oxide deposits. Econ.Geology
826 105, 641-654
827 Gumovsky A.S., Istomin N.N., Ignatiev E.K., 1984. Report on the revision work on the deposits and occurrences of the Khim-
828 Kirganik and Bystrinskoe ore zones during 1981-1984. Unpubl. Prof. Report, Kamchatgeologya, Milkovo. (in Russian)
829 Gustafson L.B., Hunt J.P., 1975. The porphyry copper deposit at El Salvador, Chile. Econ. Geology 70, 857–912
830 Hagemann S.G., Brown P.E., 1996. Geobarometry in Archean lode-gold deposits. Eur. J. Mineral. 8, 937-960
831 Halter W.E., Heinrich C.A., Pettke T., 2005. Magma evolution and the formation of porphyry Cu–Au ore fluids: evidence
832 from silicate and sulfide melt inclusions. Miner. Deposita 39, 845-863
833 Hanyu, T., Tatsumi Y., Nakai S., Chang Q., Miyazaki T., Sato K., Tani K., Shibata T., Yoshida T., 2006. Contribution of slab
834 melting and slab dehydration to magmatism in the NE Japan arc for the last 25 Myr: Constraints from geochemistry.
835 Geochem. Geophys. Geosyst. 7, Q08002
836 Harris A.C., Kamenetsky, V.S., White, N.C., van Achterbergh E., Ryan C.G., 2003. Melt inclusions in veins: Linking magmas
837 and porphyry Cu deposits. Science 302, 2109-2111
838 Harris A.C., Kamenetsky, V.S., White, N.C., Steele, D.A., 2004. Volatile phase separation in silicic magmas at Bajo de la
839 Alumbrera porphyry Cu-Au deposit, NW Argentina. Resource Geology 54, 341-356
840 Holliday J.R., Cooke D.R., 2007. Advances in geological models and exploration methods for copper ± gold porphyry
841 deposits. In: Milkereit D. (ed.), Proceedings of Exploration 2007: Fifth Internat.Conf. Min. Exploration, pp.791-809
842 Holliday, J.R., Wilson, A.J., Blevin, P.L., Tedder, I.J., Dunham, P.D., Pfitzner, M., 2002. Porphyry gold-copper mineralization
843 in the Cadia district, eastern Lachlan fold belt, New South Wales, and its relationship to shoshonitic magmatism. Miner.
844 Deposita 37, 100−116
845 Holtz F., Becker A., Freise M., Johannes W., 2001. The water-undersaturated and dry Qz-Ab-Or system revisited.
846 Experimental results at very low water activities and geological implications. Contrib. Mineral. Petrol. 141, 347-357
847 Holwell D.A., Blanks D.E. (2021). Emplacement of magmatic Cu-Au-Te(-Ni-PGE) sulfide blebs in alkaline mafic rocks of the
848 Mordor Complex, Northern Territory, Australia. Mineralium Deposita https://doi.org/10.1007/s00126-020-01015-2

Hou, T., Charlier, B., Holtz, F., Veksler, I., Zhang, Z., Thomas R., Namur O., 2018. Immiscible hydrous Fe–Ca–P melt and the origin of iron oxide-apatite ore deposits. Nature Commun. 9(1), 1415

Hourigan J.K., Solov'ev A.V., Ledneva G.V., Garver J.I., Brandon M.T., Reiners P.W., 2004. Timing of syenite intrusions on the eastern slope of the Sredinnyi Range, Kamchatka: Rate of accretionary structure exhumation. Geochemistry Internat. 42(2), 97–105

Huang M-L., Gao J-F., Bi X-W., Xu L-L., Zhu J-J., Wang D-P., 2020. The role of early sulfide saturation in the formation of the Yulong porphyry Cu-Mo deposit: Evidence from mineralogy of sulfide melt inclusions and platinum-group element geochemistry. Ore Geology Reviews, doi: https://doi.org/10.1016/j.oregeorev.2020.103644

Ignatiev E.K., Shapovalenko V.N., Chitalin A.F., Segal S.Z., 1999. Report of geological investigations conducted over the Kirganik-Sharom ore zone by BHP International Resources during 1997-1998. Unpubl. Prof. Report, Petropavlovsk-Kamchatsky. 70 p. (in Russian)

Ishihara S., 1981. The granitoid series and mineralization. Econ. Geology 75, 458-484

Jenner F.E., O'Neil H.S.C., Arculus R.J., Mavrogenes J.A., 2010. The magnetite crisis in the evolution of arc-related magmas and the initial concentration of Au, Ag and Cu. Jour. Petrol. 51, 2245-2264

Jensen E.P., Barton, M.D., 2000. Gold deposits related to alkaline magmatism. Rev. Econ. Geology 13, pp. 279-314

Jung C., Jung S., Hoffer E., Berndt J., 2006. Petrogenesis of Tertiary mafic alkaline magmas in the Hocheifel, Germany. Jour Petrology 47, 1637-1671

Kepezhinskas P., 1994. Diverse shoshonite magma series in the Kamchatka Arc: relationships between intra-arc extension and composition of alkaline magmas. Geological Society, London, Special Publications, 81(1), 249-264

Knipping J.L., Bilenker L.D., Simon A.C., Reich M., Barra F., Deditius A.P., Lundstrom C., Bindeman I., Minizaga R, 2015a. Giant Kiruna-type deposits form by efficient flotation of magmatic magnetite suspensions. Geology 43(7), 591-594

Knipping, J.L., Bilenker, L.D., Simon, A.C., Reich, M., Barra, F., Deditius, A.P., Wälle, M., Heinrich, C.A., Holtz, F., Munizaga, R., 2015b. Trace elements in magnetite from massive iron oxide-apatite deposits indicate a combined formation by igneous and magmatic-hydrothermal processes. Geochim. Cosmochim. Acta 171, 15–38

Koloskov V.A., Flerov G.B., Kovalenko D.V., 2009. Late Cretaceous–Paleocene magmatic complexes of Central Kamchatka: Geological settings and compositional features. Russian Journal of Pacific Geology 3(4), 319–337

Koloskov A.V., Flerov G.B., Seliverstov V.A., Dorendorf F., Churikova T.G., 1999. Potassic volcanoes of Central Kamchatka and the Late Cretaceous–Paleogene Kuril–Kamchatka alkaline province. Petrology 7(5), 527–543

Konnikov E.G., Chubarov V.M., Travin V.A., Matukov D.I., Sidorov E.G., 2006. The time of the origin of Ni-bearing norite-cortlandite formation in the east of the Asian continent. Geokhimiya 5, 564–570 (in Russian)

879 Kouzmanov K., Pokrovski, G.S., 2012. Hydrothermal controls on metal distribution in porphyry Cu (-Mo-Au) systems. In:
880 Hedenquist J.W., Harris M., Camus F. (eds.), Geology and Genesis of Major Copper Deposits and Districts of the World:
881 A Tribute to Richard H. Sillitoe. SEG Spec. Publ. 16, pp. 573–618
882 Kovalenko D.V., 2010. Tectonics and magmatism of Kamchatka. Lithosphere no. 3, 51-59 (in Russian)
883 Lang, J.R., Lueck, B., Mortensen, J.K., Russell, J.K., Stanley, C.R., Thompson, J.F.H., 1995. Triassic-Jurassic silica-
884 undersaturated and silica-saturated alkalic intrusions in the Cordillera of British Columbia: Implications for arc
885 magmatism. Geology 23, 451–454
886 Lang J.R., Stanley C.R., Thompson H.F.H., 1993. A subdivision of alkalic porphyry Cu-Au deposits into silica-saturated and
887 silica-undersaturated subtypes. In: Porphyry Copper-Gold Systems of British Columbia. MDRU, University of British
888 Columbia, Annual Technical Report - Year 2, pp. 3.2-3.14
889 LeFort D., Hanley J., Guillong M., 2011. Subepithermal Au-Pd mineralization associated with an alkalic porphyry Cu-Au
890 deposit, Mount Milligan, Quesnel Terrane, British Columbia, Canada. Econ. Geology 106, 781-808
891 Le Maitre R.W., Bateman P., Dudek A., Keller J., Lameyre J., Le Bas M.J., Sabine P.A., Schmid R., Sorensen H., Streckeisen
892 A., Wooley A.R., Zanettin B., 1989. A classification of igneous rocks and glossary of terms. Blackwell, Oxford, 193 p.
893 Lickfold V., Cooke D.R., Crawford A.J., Fanning C.M., 2007. Shoshonitic magmatism and the formation of the Northparkes
894 porphyry Cu-Au deposits, New South Wales. Austral. J. Earth Science 54, 417-444
895 Logan J.M., 2005. Alkaline magmatism and porphyry Cu-Au deposits at Galore Creek, northwestern British Columbia. B.C.
896 Ministry of Energy, Mines and Petroleum Resources, Geological Fieldwork, paper 2005-1, p. 237-248
897 Logan J.M., Mihalynuk M.G., 2014. Tectonic controls on Early Mesozoic paired alkaline porphyry deposit belts (Cu-Au ± Ag-
898 Pt-Pd-Mo) within the Canadian Cordillera. Econ. Geology 109, 827-858
899 Ludwig, K.R., 2003. User's manual for Isoplot 3.00: A Geochronological Toolkit for Microsoft Excel, 4. Berkeley
900 Geochronology Center Special Publication.
901 MacLean W.H., Barrett T.J., 1993. Lithogeochemical techniques using immobile elements. Jour Geochem Explor 48, 109-133
902 Maniar P.D., Piccoli P.M., 1989. Tectonic discrimination of granitoids. Geol. Soc. Amer Bull 101, 635-643
903 Mao M., Rukhlov A.S., Rowins S.M., Spence J., Coogan L.A., 2016. Apatite trace element compositions: A robust new tool
904 for mineral exploration. Econ. Geology 111, 1187-1222
905 Masterman G.J., Cooke D.R., Berry R.F., Walshe J.L., Lee A.W., Clark A.H., 2005. Fluid chemistry, structural setting, and
906 emplacement history of the Rosario Cu-Mo porphyry and Cu-Ag-Au epithermal veins, Collahuasi District, Northern
907 Chile. Econ. Geol. 100, 835-862
908 McDonough W.F., Sun, S.-S., 1995. The composition of the Earth. Chemical Geology 120, 223-253

Meen J.K., 1987. Formation of shoshonites from calc-alkaline basalt magmas: geochemical and experimental constraints from the type locality. Contrib. Mineral. Petrol. 97, 333–351

Mernagh T.P., Mavrogenes J., 2019. Significance of high temperature fluids and melts in the Grasberg porphyry copper‐gold deposit. Chem. Geology 508, 210-224

Middlemost E.A.K., 1997. Magmas, Rocks and Planetary Development. Longman, Harlow, 299 p.

Mihalasky M.J., Ludington S., Alexeiev D.V., Frost T.P., Light T.D., Briggs D.A., Hammarstrom J.M., Wallis, J.C., Bookstrom A.A., Panteleyev A., 2015. Porphyry copper assessment of northeast Asia-Far East Russia and Northeasternmost China. U.S. Geological Survey Scientific Investigations Report 2010–5090–W, 104 p.

Misco J., Tosdal R.M., Bissig T., Chamberlian C.M., Simpson K.A., 2014. Hydrothermal alteration and mineralization of the Galore Creek alkalic Cu-Au porphyry deposit, northwestern British Columbia, Canada. Econ. Geology 109, 891-914

Moritz R., Rezeau H., Ovtcharova M., Tayan R., Melkonyan R., Hovamkimyan S., Ramazanov V., Selby D., Ulianov A., Chiaradia M., Putlitz B., 2016. Long-lived, stationary magmatism and pulsed porphyry systems during Tethyan subduction to postcollision evolution in the southernmost Lesser Caucasus, Armenia and Nakhitchevan. Gondwana Research 37, 465-503

Muller D., Groves D.I., 2019. Potassic igneous rocks and associated gold-copper mineralization. Springer International Publishing AG, part of Springer Nature, Berlin-Heidelberg-New York, 5th edition. 398 p.

Mungall J.F., Long K., Brenan J.M., Smythe D., Naslund H.R., 2018. Immiscible shoshonitic and Fe-P-oxide melts preserved in unconsolidated tephra at El Laco volcano, Chile. Geology 46(3), 255-258

Mutschler F.E., Mooney T.C., 1993. Precious-metal deposits related to alkalic igneous rocks: Provisional classification, grade-tonnage data and exploration frontiers. In: Kirkham R.V., Sinclair W.D., Thorpe R.I., Duke, J.M. (eds.), Mineral Deposit Modeling: Geological Association of Canada, Special Paper 40, p. 479-520

Nadoll, P., Angerer, T., Mauk, J.L., French, D., Walshe, J., 2014. The chemistry of hydrothermal magnetite: A review. Ore Geol. Rev. 61(5), 1–32

Nokleberg W.J., Bundtzen T.K., Dawson K.M., Eremin R.A., Goryachev N.A., Koch R.D., Ratkin V.V., Rozenblum I.S., Shpikerman V.I., Frolov Y.F., Gorodinsky M.E., Melnikov V.D., Ognyanov N.V., Petrachenko E.D., Petrachenko R.I., Pozdeev A.I., Ross K.V., Wood D.H., Grybeck D., Khanchuk A.I., Kovbas L.I., Nekrasov I.Y., Sidorov A.A., 1996. Significant metalliferous and selected non-metalliferous lode deposits and placer districts for the Russian Far East, Alaska, and the Canadian Cordillera. U.S. Geological Survey Open-File Report 96-513-A, 385 p.

937 Nokleberg, W.J., Parfenov, L.M., Monger, J.W.H., Norton, I.O., Khanchuk, A.I., Stone, D.B., Scholl, D.W., Fujita, K., 1998.
938 Phanerozoic tectonic evolution of the Circum-North Pacific. US Department of the Interior, Open-File Report 98-574.
939 U.S. Geological Survey. 125 pp.
940 Pacey A., Wilkinson J.J., Owens J, Priest D., Cooke D, Millar I.L., 2019. The anatomy of an alkalic porphyry Cu-Au system:
941 Geology and alteration at Northparkes Mines, New South Wales, Australia. Econ. Geology 114, 441-472
942 Pass, H.E., Cooke, D.R., Davidson, G., Maas, R., Dipple, G., Rees, C., Ferreira, L., Taylor, C., Deyell, C.L., 2014. Isotope
943 geochemistry of the Northeast zone, Mount Polley alkalic Cu-Au-Ag porphyry deposit, British Columbia: A case for
944 carbonate assimilation. Econ. Geology 109, 859-890
945 Pearce, J.A., Peate, D.W., 1995. Tectonic implications of the composition of volcanic arc magmas. Annu. Rev. Earth Planet.
946 Sci. 23, 251–285
947 Peccerillo A., Taylor S.R., 1976. Geochemistry of Eocene calc-alkaline volcanic rocks from the Kastamonu area, Northern
948 Turkey. Contrib. Mineral. Petrol. 58, 63–81
949 Perepelov A.B., 2014. Cenozoic magmatism of Kamchatka during the epochs of changing geodynamic environments. Sc. D.
950 Dissertation. Institute of Geochemistry, SB RAS, Irkutsk. 361 p. (in Russian)
951 Pettke, T., Oberli, F., Heinrich, C.A., 2010. The magma and metal source of giant porphyry-type ore deposits, based on lead
952 isotope microanalysis of individual fluid inclusions. Earth Planet. Sci. Lett. 296, 267–277
953 Pollard P.J., Taylor R.G., Peters L., 2005. Ages of intrusion, alteration, and mineralization at the Grasberg Cu-Au deposit,
954 Papua, Indonesia. Econ. Geol. 100, 1005-1020
955 Polokhov V.P., Volynets O.N., 1968. The dike suite and mineralization in the Kirganik Pass area (Central Range, Kamchatka).
956 In: Favorskaya M.A. (ed.), Formations and Facies of the Late Cretaceous and Cenozoic Igneous Suites of Central
957 Kamchatka. Moscow, Nauka Publishing, pp. 141-174 (in Russian)
958 Redmond P.B., Einaudi M.T., 2010. The Bingham Canyon porphyry Cu-Mo-Au deposit. I. Sequence of intrusions, vein
959 formation, and sulfide deposition. Econ. Geology 105, 43-65
960 Richards J.P., 1995. Alkalic-type epithermal gold deposits - a review. Min. Assoc. Canada Short Course Series 23, 367-400
961 Richards J.P, 2011. Magmatic to hydrothermal metal fluxes in convergent and collided margins. Ore Geology Rev. 40, 1-26
962 Richards, J.P., Lypez, G.P., Zhu, J.J., Creaser, R.A., Locock, A.J., Mumin, A.H., 2017. Contrasting tectonic settings and sulfur
963 contents of magmas associated with Cretaceous porphyry Cu±Mo±Au and intrusion-related iron oxide Cu-Au deposits in
964 Northern Chile. Econ. Geology 112 (2), 295-318
965 Richards, J.P., Mumin, A.H., 2013a. Magmatic-hydrothermal processes within an evolving Earth: Iron oxide-copper-gold and
966 porphyry Cu ± Mo ± Au deposits. Geology 41, 767–770

967 Richards, J.P., Mumin, A.H., 2013b. Lithospheric fertilization and mineralization by arc magmas: Genetic links and secular
968 differences between porphyry copper ± molybdenum ± gold and magmatic-hydrothermal iron oxide copper-gold deposits.
969 SEG Special Publication, no. 17, pp. 277–299
970 Roedder E., 1984. Fluid inclusions in minerals. Rev. Mineral. 12, 644 p.
971 Schairer, J.F., Yoder, H.S., Jr. 1960. The nature of residual liquids from crystallization, with data on the system diopside-
972 nepheline-silica. Amer. Jour. Sci. 258-A, 273-283
973 Seedorff E., Dilles J., Proffett J.J., Einaudi M., Zurcher L., Stavast W., Johnson D., Barton M., 2005. Porphyry deposits:
974 charateristics and origin of hypogene features. Econ. Geology 100, 251–298
975 Seedorff, E., Barton, M.D., Stavast, W.J.A., Maher, D.J., 2008. Root zones of porphyry systems: Extending the porphyry
976 model to depth. Econ. Geology 103, 939−956
977 Shatova N.V., Molchanov A.V., Terekhov A.V., Shatov V.V., Petrov O.V., Sergeev S.A., Prasolov E.M., Dvornik G.P.,
978 Leontev L.I., 2019. The Ryabinovoe copper-gold-porphyry deposit (Southern Yakutia): Geology, noble gases isotope
979 systematics, and isotopic (U-Pb, Rb-Sr, Re-Os) dating of wallrock alteration and ore-forming processes. Regional
980 Geology and Metallogeny 77, 75–97 (in Russian)
981 Shepherd, T.J., Rankin, A.H., Alderton, D.H.M., 1985. A practical guide to fluid inclusion studies. Glasgow-London, Blackie
982 & Son, 239 p.
983 Sidorov E.G., Ignatiev E.K., Chubarov V.M., 2017. First find of platinum group metals in the ore of Kirganik copper-porphyry
984 deposit (Kamchatka). Doklady Earth Sciences 475(2), 883-886
985 Sillitoe, R.H., 1973. The tops and bottoms of porphyry copper deposits. Econ. Geology 68, 799–815
986 Sillitoe R.H., 2002. Some metallogenic features of gold and copper deposits related to alkaline rocks and consequences for
987 exploration. Miner. Deposita 37, 4-13
988 Sillitoe R.H., 2010. Porphyry copper systems. Econ. Geology 105, 3-41
989 Simon A.S., Pettke T., Candela P.A., Piccoli P.M., Heinrich C.A., 2006. Copper partitioning in a melt–vapor–brine–
990 magnetite–pyrrhotite assemblage. Geochim. Cosmochim. Acta 70, 5583–5600
991 Simpson, R., 2014. Sulfide inclusions in zircon and their significance to understanding the evolution of copper porphyries in
992 the Macquarie Arc, New South Wales, Bachelor of Science (Hons.), School of Earth and Environmental Sciences,
993 University of Wollongong, 197 p.
994 Slyadnev B.I., Shapovalenko V.N., Krikun N.A., Poletaeva A.A., Rotman V.K., Sidorenko V.I., Sidorov E.G., Surikov S.N.,
995 Khasanov S.G., 2006. Explanatory Notes to the State Geological Map of the Russian Federation, 1:1000000 scale (third
996 generation). Kamchatka-Koryak Series, N-57 Sheet. VSEGEI Publishing, Petropavlovsk-Kamchatsky. 376 p. (in Russian)

997 Soloviev S.G., 2014. Metallogeny of Shoshonitic Magmatism. Moscow, Scientific World Publishing. V. 1. 528 p., V. 2. 472 p.
998 (in Russian)
999 Soloviev S.G., Kryazhev S.G., Avilova O.V., Andreev A.V., Girfanov M.M., Starostin I.A., 2019a. The Lazurnoe deposit in
1000 the Sobolinoe area, Sikhote-Alin, Eastern Russia: Combined shoshonite-related Cu-Au-Mo porphyry and reduced
1001 intrusion-related Au mineralization in a post-collisional setting. Ore Geology Reviews 112, paper # 103063, p.1-26
1002 Soloviev S.G., Kryazhev S.G., Dvurechenskaya S.S., Vasyukov V.E., Shumilin D.A., Voskresensky K.I., 2019b. The
1003 superlarge Malmyzh porphyry Cu-Au deposit, Sikhote-Alin, Eastern Russia: Igneous geochemistry, hydrothermal
1004 alteration, mineralization, and fluid inclusion characteristics. Ore Geology Reviews 113, paper # 103112, p.1-27
1005 Stefanova, E., Driesner, T., Zajacz, Z., Heinrich, C.A., Petrov, P., Vasilev, Z., 2014, Melt and fluid inclusions in hydrothermal
1006 veins: The magmatic to hydrothermal evolution of the Elatsite porphyry Cu-Au deposit, Bulgaria. Econ. Geology 109,
1007 1359–1381
1008 Stepanov V.A., Trukhin Y.P., 2007. Age of the Shanuch copper-nickel deposit in Kamchatka. Doklady Earth Sci. 417(1), 84-
1009 86
1010 Student, J.J., Bodnar, R.J., 2004. Silicate melt inclusions in porphyry copper deposits: Identification and homogenization
1011 behavior. Can. Mineral. 42, 1563–1600
1012 Sun S.-S., McDonough W.F., 1989. Chemical and isotopic systematics of oceanic basalts: Implications for mantle composition
1013 and processes. Geological Society of London, Special Publication 42, 313–345
1014 Sun W.D., Huang R.F., Li H., Hu Y.B., Zhang C.C., Sun S.J., Zhang L.P., Ding X., Li C.Y., Zartman R.E., Ling M.X., 2015.
1015 Porphyry deposits and oxidized magmas. Ore Geology Rev. 65, 97-131
1016 Thiéblemont D., Tegyey M., 1994. Une discrimination géochimique des roches différenciées témoin de la diversité
1017 d'origlisboaine et de situation tectonique des magmas calcoalcalins. Comptes Rendus de l'académie des Sciences Paris
1018 319, 87–94
1019 Thompson J.F.H., Lang J.R., Stanley C.R., 2001. Platinum group elements in alkaline porphyry deposits, British Columbia.
1020 Exploration and Mining in British Columbia, p.57-64
1021 Tsuruoka, S., 2017. The evolution of hydrothermal fluids from the deep porphyry environment to the shallow epithermal
1022 environment. Ph.D. Thesis, Golden, Colorado, Colorado School of Mines, 182 p.
1023 Tsvetkov, A.A., Volynets, O.N., Bailey, J.C., 1993. Shoshonites of the Kurile-Kamchatka island arc. Petrology 1(2),
1024 123-151
1025 Vlasov G.M., Vasilevsky M.M., 1964. Hydrothermally Altered Rocks in Central Kamchatka, Their Mineralization and
1026 Regularities of Spatial Distribution. Moscow, Nedra Publishing. 220 p. (in Russian)

Williams, P.J., Barton, M.D., Johnson, D.A., Fontbote, L., de Haller, A., Mark, G., Oliver, N.H.S., Marschik, R., 2005. Iron oxide copper-gold deposits: Geology, space-time distribution, and possible modes of origin: Econ. Geology 100th Anniv. Volume, p. 371–405

Wilkinson J.J., 2013. Triggers for the formation of porphyry ore deposits in magmatic arcs. Nature Geoscience 6, 917-925

Wilson A.J., Cooke D.R., Harper B.L., 2003. The Ridgeway gold-copper deposit; a high-grade alkalic porphyry deposit in the Lachlan fold belt, New South Wales, Australia. Econ. Geology 98, 1637–1666

Wolfe R.C., Cooke D.R., 2011. Geology of the Didipio region and genesis of the Dinkidi alkalic porphyry Cu-Au deposit and related pegmatites, Northern Luzon, Philippines. Econ. Geology 106, 1279-1315

Yakubchuk A.S., 2009. Revised Mesozoic–Cenozoic orogenic architecture and gold metallogeny in the northern Circum-Pacific. Ore Geology Reviews 35, 447-454

Zhang D., Audetat A., 2017. What caused the formation of the giant Bingham Canyon porphyry Cu-Mo-Au deposit? Insights from melt inclusions and magmatic sulfides. Econ. Geology 112, 221-244

Zhao J., Zhou M., 2009. Secular evolution of the Neoproterozoic lithospheric mantle underneath the northern margin of the Yangtze block, South China. Lithos 107, 152-168

Zvezdov V.S., 1997. The geology and genesis of the Kirganik copper-gold deposit in Kamchatka. National Geology, no. 5, p.13-17 (in Russian)

FIGURE CAPTIONS

FIG. 1. Regional tectonic setting of the Kirganik and other porphyry Cu-Au porphyry and epithermal Au (Au-Ag) deposits and prospects on the Kamchatka Peninsula (after Nokleberg at al., 1996, 1998; Goryachev et al., 2010; Slyadnev et al., 2006).

FIG. 2. Geological setting of the Kirganik prospect area in Central Kamchatka (modified after Ignatiev et al., 1999; Slyadnev et al., 2006).

FIG. 3. Geological map of the Kirganik prospect (A) and an enlarged map showing principal mineralized and hydrothermal alteration zones (B) (modified after Ignatiev et al., 1999).

1056

1057 FIG. 4. Cross-sections of the Kirganik prospect, with the principal drill holes, main alteration and mineralized zones,
1058 and selected historical (1976-1984) mineralized intercepts in trenches and drill holes (compiled and interpreted by the
1059 authors). For the legend see Fig. 3. Dashed orange line at the upper section indicates a possible boundary between
1060 pyroxene-dominant and biotite-dominant calc-potassic and potassic alteration assemblages.

1061

1062 FIG. 5. Photographs showing some typical features of the Late Cretaceous (to Paleocene ?) igneous rocks at the
1063 Kirganik prospect. A. Monzogabbro-porphyry. B. Monzodiorite-porphyry. C. Monzonite-porphyry. D. Monzonite-
1064 porphyry with calc-potassic and potassic alteration overprints. E-G. Possible younger (intramineral) monzonitic
1065 phases (?) containing K-feldspar-dominant clasts (xenoliths) with or without Cu-sulfides. H. Equigranular to
1066 weakly-porphyritic syenite. I. Syenite-porphyry microdikes ("vein-dikes") and adjacent branching monomineralic
1067 K-feldspar "injections". J. Syenite cements angular, partially replaced fragments of host rocks and evolves into
1068 narrow zones of magmatic replacement along outer contacts. K. Trachytic syenite-porphyry with reddened
1069 (hematite-dusted) K-feldspar phenocrysts. L. Sharp contact of trachytic syenite-porphyry and another, possibly
1070 nearly coeval (with no quenching on the contact) rock with minor elongated K-feldspar phenocrysts, mostly tabular
1071 K-feldspar phenocrysts, and no trachytic texture; both are subjected to reddening (hematite dusting) of K-feldspar
1072 phenocrysts. M-N. Trachytic syenite-porphyry microdikes cutting zones of potassic alteration. O. Trachytic
1073 syenite-porphyry intrudes blocky K-feldspar aggregate associated with syenite. P. Fragments (xenoliths) of
1074 potassic-altered rocks with bornite (Bn) in trachytic syenite-porphyry. Abbreviation: Bn – bornite.

1075

1076 FIG. 6. Plots illustrating the chemistry of igneous rocks from the Kirganik prospect. (A) Al_2O_3 vs. TiO_2 diagram
1077 showing immobility of Al and Ti in the rock samples (MacLean and Barrett, 1993). (B) SiO_2 vs. (K_2O+Na_2O)
1078 diagram for chemical compositions of intrusive rocks (after Le Maitre et al., 1989; Middlemost, 1997). (C) SiO_2 vs.
1079 K_2O diagram (after Peccerillo and Taylor, 1976; Le Maitre et al., 1989). (D) Al/(Na+K) vs. Al/(Ca+Na+K)
1080 diagram defining the alkaline, metaluminous and peraluminous igneous rocks as well as the I- and S-types of
1081 granites (after Maniar and Piccoli, 1989; Chappell and White, 1992). (E) Diagram showing compositional fields of
1082 shoshonitic rocks formed in within-plate (WIP), continental arc (CAP) and post-collisional arc (PAP), initial

1083 oceanic arc (IAP) and late oceanic arc (LOP) tectonic environments (Muller and Groves, 2019). (F) Nb/Zr vs. Zr
1084 diagram showing compositional fields of igneous rocks formed in subduction-related, collision-related and
1085 intraplate tectonic environments (Thiéblemont and Tegyey, 1994). (G) Primitive mantle-normalized extended trace
1086 element spider diagrams (normalization with respect to Sun and McDonough, 1989) and rare earth element
1087 chondrite-normalized diagrams (normalization with respect to McDonough and Sun, 1995). The individual rock
1088 compositions are from Table 2.
1089
1090 FIG. 7. Sequence of hydrothermal alteration assemblages and intrusive phases at the Kirganik prospect.
1091
1092 FIG. 8. Photographs showing some typical features of potassic alteration assemblages at the Kirganik prospect. A.
1093 Central ("core") pyroxene zones in syenite-porphyry microdike and dike-vein. B. Zone of calc-potassic alteration
1094 with dominant K-feldspar and minor pyroxene (after altered syenite ?). C. Zone of calc-potassic alteration with
1095 dominant pyroxene and minor K-feldspar and magnetite (thin polished slab, transmitted light). D. Pyroxene-apatite
1096 veinlets in massive K-feldspar-pyroxene alteration zone. E. Andehral apatite, magnetite and fine-grained pyroxene
1097 in zone of calc-potassic alteration (thin section, transmitted light). F. Veined and patchy replacement by potassic
1098 alteration assemblages. G. Zone of pervasive fine-grained K-feldspar alteration is partially recrystallized into
1099 coarser-grained K-feldspar aggregates, with introductions of biotite, magnetite and Cu-sulfides (bornite,
1100 chalcopyrite). H. Medium- to coarse-grained potassic (K-feldspar-dominant) alteration with biotite, pyroxene,
1101 magnetite and bornite segregations. I. Biotite-magnetite-bornite overprint of K-feldspar-pyroxene aggregate. J.
1102 Coarse-grained to pegmatite-like zone of potassic alteration (K-feldspar+biotite) with magnetite and bornite. K.
1103 Coarse biotite aggregates with magnetite and euhedral apatite (thin section, transmitted light). L. Coarse biotite
1104 segregations with magnetite and Cu-sulfides (oxidized) in fine-grained K-feldspar-biotite-magnetite alteration zone
1105 (thin section, transmitted light). M. Coarse biotite aggregate with magnetite and Cu-sulfides (oxidized) (thin
1106 section, transmitted light). N. Hydrothermal breccia with fragments (clasts) of potassic-altered rocks and
1107 magnetite+albite cement. Abbreviations: Px – pyroxene, Ap – apatite, Bt – biotite, Mag – magnetite, K-Fsp – K-
1108 feldspar.
1109

1110 FIG. 9. Photomicrographs showing relationships of Cu-sulfide minerals in potassic alteration assemblages at the
1111 Kirganik prospect (polished sections, reflected light). A-C. Rounded and droplet-like bornite (with chalcopyrite
1112 exsolution) aggregates in magnetite (A-B) and K-feldspar (C). D. Bornite (with exsolved chalcocite) dissemination
1113 in K-feldspar-biotite aggregate. E. Bornite closely associated with coarse biotite. F-G. Bornite replacing magnetite
1114 and replaced by chalcopyrite. H. Chalcopyrite replaces bornite with exsolved chalcopyrite. I-L. Native gold in
1115 bornite and chalcopyrite. Abbreviations: Bt – biotite, Mag – magnetite, Bn – bornite, Ccp – chalcopyrite, Au –
1116 native gold.
1117
1118 FIG. 10. Photographs showing some typical features of propylitic and phyllic alteration at the Kirganik prospect.
1119 A. “Outer” propylitic alteration (chlorite+magnetite+albite) overprinting mafic volcanic rock. B. Hydrothermal
1120 breccia with pyrite matrix and trachytic syenite-porphyry fragments. C. Chlorite-magnetite veinlets intersecting K-
1121 dominant potassic alteration zone. D. Zone of K-feldspar-dominant potassic alteration is brecciated and cemented
1122 by chlorite-epidote-magnetite-pyrite aggregates. E. Chlorite-albite-magnetite aggregate. F. Quartz-Fe-carbonate-
1123 sericite veinlets in zones of quartz-sericite (phyllic) alteration overprinting Oligocene-Miocene diorite-porphyry
1124 dike.
1125
1126 FIG. 11. Rb-Sr isochron ages of K-feldspar, biotite and whole rock representing potassic alteration assemblages
1127 from the Kirganik prospect.
1128
1129 FIG. 12. Types of fluid inclusions in apatite from calc-potassic (pyroxene-K-feldspar) and potassic (biotite-K-
1130 feldspar) alteration assemblages at the Kirganik prospect. A-F. Melt inclusions in apatite from calc-potassic
1131 (pyroxene-K-feldspar) alteration assemblage (B, D, F – larger views). G-L. Liquid-gaseous type 1 fluid inclusions
1132 in apatite from calc-potassic (pyroxene-K-feldspar) alteration assemblage (H, J, L – larger views). M-P. Liquid-
1133 gaseous type 2 fluid inclusions in apatite from potassic (biotite-K-feldspar) alteration assemblage. Abbreviations:
1134 G – gas, Ap – apatite, Px – pyroxene, Bt – biotite, Mag - magnetite.
1135

1136 FIG. 13. Geochemical diagrams showing conditions of magma generation and evolution of the Kirganik volcanic-
1137 plutonic suite. (A) Dy/Yb vs. La/Yb diagram showing compositional fields of mafic alkaline magmas generated
1138 under amphibole-garnet and amphibole-spinel peridotite melting, with the respective proportions of mixing
1139 between these melts (Jung et al., 2006). Numbers on model curves indicate the percent melting. Points at
1140 80Grt/20Sp, 60Grt/40Sp and 40Grt/60Sp indicate mixing proportions of melts from amphibole-garnet peridotite
1141 (e.g., 80 vol.%) with melts from amphibole-spinel peridotite (e.g., 20 vol.%). Note that some rocks plot outside the
1142 model fields, thus indicating the incompatibility of these rock compositions to the modelled solely mantle source.
1143 (B) Sm/Yb vs. La/Yb diagram showing compositional fields of mafic alkaline magmas generated under garnet to
1144 spinel lherzorite melting (Zhao and Zhou, 2009). Numbers on model curves indicate the percent melting. Note that
1145 some rocks plot outside the model fields, thus indicating the incompatibility of these rock compositions to the
1146 modelled solely mantle source. (C) Th/Yb vs. Ba/La diagram discriminating fluid-derived vs. slab-derived
1147 metasomatic processes, which contributed to the overall metasomatic enrichment of the deep-seated magma source
1148 (Hanyu et al., 2006). (D) La/Sm vs. Sm/Yb diagram displaying approximate stability thresholds of clinopyroxene,
1149 amphibole and garnet stabilities in mantle melt residues (Moritz et al., 2016). (E) Dy/Yb vs. SiO_2 diagram
1150 displaying amphibole and garnet fractionation trends (Davidson et al., 2007). (F) Sr vs. Ba diagram showing
1151 dominant trends of crystallization differentiation. Abbreviations: CPx – clinopyroxene, Amp – amphibole, Grt –
1152 garnet, Bt – biotite, Pl – plagioclase, Ksp – K-feldspar. The individual rock compositions are from Table 2.
1153
1154 FIG. 14. Pressure estimates for the formation conditions of calc-potassic and potassic alteration at the Kirganik
1155 prospect using the type 1 and 2 fluid inclusion (FI) homogenization temperatures (Table 6) and the entrapment
1156 temperatures assumed by the analogy with other porphyry Cu-Au deposits. The liquid-gas curves and isochors
1157 (corresponding to various salinities, wt.% NaCl) are from Bodnar and Vityk (1994).
1158
1159 FIG. 15. Estimated pressure and temperature conditions and evolutional paths for different fluid inclusion types in
1160 potassic alteration assemblages at the Kirganik prospect, with composition of different fluid inclusion types as a
1161 function of depth and temperature (the principal diagram after Bodnar et al., 1985; Fournier, 1999). Vapor pressure
1162 curves for H_2O-NaCl solutions at 0-70 wt.% NaCl and the three-phase (L+V+H) curve are shown after Atkinson

(2002) and Becker et al. (2008). The isochors (corresponding to various salinities, wt.% NaCl) are from Bodnar and Vityk (1994). Dashed line represents water-saturated granite solidus (Holtz et al., 2001). PT-fields for the major fluid inclusion types and possible evolutional paths for fluids (arrows) are shown. L, V, H – liquid, vapor, and halite phases, respectively. CP – line of critical points.

FIG. 16. Models showing possible interpretations of geological setting of the Kirganik prospect. A. A model implying a larger and more differentiated causative intrusion situated at a greater depth below the known mineralized zones. B. A model implying the control of hydrothermal alteration and mineralization by flat-lying (possibly thrust-fault-like) structures. C. A model implying initially subvertical setting, with finger-like intrusive apophyses and alternating lenticular zones of hydrothermal alteration and mineralization; post-mineral deformations has led to the ~90^{o} tilt of the geology. For the legend see Fig. 3.

FIG. 17. Plots of V + Ti vs. Al + Mn (A) and Ti +V vs. Ni/ (Cr + Mn) (B) for magnetite from calc-potassic and potassic alteration assemblages at the Kirganik prospect (diagrams after Nadoll et al., 2014). The data from Kirganik appear to expand the field of the Cu-Au porphyry-related magnetite compositions further toward higher Ti and V contents. The individual mineral compositions are from Table 5.

Highlights

The prospect is related to an island-arc shoshonitic series
The prospect geology is interpreted toward initially subvertical mineralized intrusions, then tilted
Fluid inclusion data indicate a homogenous low-salinity aqueous fluid
The prospect represents a deep level of a silica-undersaturated alkalic porphyry Cu-Au system

We the undersigned declare that this manuscript is original, has not been published before and is not currently being considered for publication elsewhere.

We confirm that the manuscript has been read and approved by all named authors and that there are no other persons who satisfied the criteria for authorship but are not listed. We further confirm that the order of authors listed in the manuscript has been approved by all of us.

We understand that the Corresponding Author is the sole contact for the Editorial process. He/she is responsible for communicating with the other authors about progress, submissions of revisions and final approval of proofs.

We confirm that there is no conflict of interest to declare.

Signed by the corresponding author:

Serguei Soloviev

June 22, 2020

Table 1. Major petrographic features of the Late Cretaceous (to Paleocene ?) intrusive rocks from the Kirganik prospect

Intrusive phase	Rocks	Petrography
1	Monzogabbro-porphyry (small stocks and dikes)	Medium- to fine-grained mafic (dark-grey to dark greenish-grey) porphyritic rock composed of clinopyroxene (50-70 vol.%), K-feldspar (orthoclase; 20-45 vol.%), plagioclase (3-5 vol.% to 10-15 vol.% in expense of K-feldspar), amphibole (0-10 vol.%), and biotite (5-10 vol.%). Rare orthopyroxene and olivine (forsterite) are present in some varieties, with orthopyroxene rimming olivine and in turn rimmed by clinopyroxene (Flerov and Koloskov, 1976). Phenocrysts (1-3 mm to 5-6 mm) totalling 25-40 vol.% are represented by clinopyroxene (Ti-augite to aegirine-augite to diopside-augite from centre to rims of the phenocrysts), locally K-feldspar and/or plagioclase. Isometric aggregates of sodalite and albite as well as K-feldspar+sodalite up to 5 mm across (possibly after leucite) are locally present. Small "vugs" filled with carbonate (calcite), clinopyroxene and locally apatite are present. Accessory minerals: acicular apatite, Ti-magnetite, zircon, titanite.
2	Monzodiorite-porphyry ("pyroxene-biotite gabbro", after Flerov and Koloskov, 1976) (dikes)	Medium- to fine-grained mafic to mesocratic (dark-grey to greenish-grey) weakly-porphyritic rock composed of clinopyroxene (aegirine-augite; 15-20 vol.%), dark-brown biotite (10-15 vol.%), amphibole (0-10 vol.%), K-feldspar (orthoclase; 10-20 vol.%) and plagioclase (20-30 vol.%). Magnetite is abundant (5-10 vol.%). Trace olivine (forsterite) and/or orthopyroxene are present as relict microinclusions in clinopyroxene. Small phenocrysts are represented by clinopyroxene and plagioclase. Plagioclase phenocrysts are zoned from labradorite (50-60 mol.% anorthite) in the core to andesine (35-50 mol.% anorthite) in the rims. Smaller plagioclase crystals in the groundmass are andesine (30-40 mol.% anorthite). Mafic (clinopyroxene-dominant) enclaves are widespread. Accessory minerals: magnetite, titanite, apatite and zircon.
3	Monzonite-porphyry (dikes)	Medium- to fine-grained mesocratic (grey to greenish-grey) equigranular to weakly-porphyritic rock composed of clinopyroxene (aegirine-augite; 5-15 vol.%), amphibole (5-10 vol.%), dark-brown to reddish-brown biotite (5-10 vol.%), K-feldspar (orthoclase) and plagioclase. Small plagioclase phenocrysts are zoned from andesine-labradorite (with 40-50 mol.% anorthite) in the core to andesine (with 30-40 mol.% anorthite) in the rims. Opposite (from anorthite-poor core to anorthite-rich rims) zonation is locally observed. Smaller plagioclase crystals in the groundmass are oligoclase-andesine (with 25-40 mol.% anorthite). Mirmekites and graphic intergrowths of K-feldspar and plagioclase occur locally. Accessory minerals: magnetite, titanite, apatite and zircon. Mafic (clinopyroxene-biotite) enclaves are widespread.
4	Syenite to syenite-porphyry (dikes, microdikes, veins, magmatic breccia cement)	Medium- to fine-grained mesocratic to leucocratic (grey to light-grey) porphyritic to equigranular rock composed of dominant blocky, locally megacrystic K-feldspar (orthoclase) (50-90 vol.%), minor plagioclase (5-15 vol.%) and mafic minerals including clinopyroxene (aegirine-augite; 5-20 vol.%), green to brownish-green amphibole (5-10 vol.%), rarely biotite (0-10 vol.%). Phenocrysts are represented by tabular twinned K-feldspar. Accessory minerals include magnetite, titanite, allanite, apatite and zircon. Syenite dikes are accompanied by wider fenite-like halos of porphyroblastic K-feldspar and branching monomineralic K-feldspar "injections". Clast- to matrix-supported magmatic breccias are present, with syenite matrix and angular fragments of volcanic and earlier (mafic) plutonic rocks.
5	Trachytic syenite-porphyry (to trachytic phonotephrite-porphyry ?) (subvolcanic intrusions)	Medium- to fine-grained mesocratic (grey to greenish-grey to pinkish-grey) sharply-porphyritic rock composed of minor (~10-20 vol.%) to abundant (>80 vol.%) elongated, "noodle-like" twinned K-feldspar phenocrysts varying from 1x5 mm to 1x6 cm, locally with a flow texture. Small clinopyroxene (diopside) (10-20 vol.%) and amphibole (5-10 vol.%) phenocrysts are also present. The fine-grained groundmass is composed of K-feldspar (5-50 vol.%), plagioclase (5-10 vol.%), biotite (0-5 vol.%), magnetite (~5 vol.%); minor calcite, analcime and possibly trace nepheline are present. Small "vugs" filled with calcite are locally present. Amount of K-feldspar phenocrysts changes gradually to abruptly, the latter suggesting multiple within-chamber intrusions. Accessory minerals: magnetite, titanite, allanite, apatite and zircon.

Table 2. Chemical composition of the least altered Late Cretaceous (to Paleocene ?) igneous rocks from the Kirganik prospect (wt.%, ppm)

	Monzogabbro-porphyry			Monzodiorite-porphyry			Monzonite-porphyry		Syenite to syenite-porphyry		Trachytic syenite-porphyry		
	1	2	3	4	5	6	7	8	9	10	11	12	13
wt.%													
SiO_2	47.24	47.59	48.65	52.14	52.19	52.55	54.81	57.20	57.48	59.31	50.43	51.40	53.62
TiO_2	0.47	0.61	0.52	0.78	0.87	0.80	0.75	0.63	0.47	0.40	0.64	0.62	0.65
Al_2O_3	15.32	14.22	14.50	15.54	15.73	15.78	15.20	15.82	15.91	17.05	15.80	15.92	15.71
Fe_2O_3	5.89	6.30	5.87	4.29	5.61	4.84	4.57	4.23	3.22	2.12	4.43	4.34	4.11
FeO	4.14	5.85	4.19	4.61	3.93	4.24	4.41	3.84	3.40	2.62	4.68	4.59	4.32
MnO	0.25	0.23	0.22	0.18	0.20	0.18	0.16	0.16	0.15	0.14	0.19	0.18	0.18
MgO	8.54	7.14	7.03	5.12	5.18	5.01	4.81	4.54	4.45	2.34	4.70	4.56	4.20
CaO	12.45	11.43	11.36	7.28	7.48	7.32	6.44	6.01	3.68	4.20	6.67	6.50	7.12
Na_2O	1.54	1.69	1.66	4.25	3.61	3.13	3.46	3.27	3.79	3.85	2.59	2.91	3.14
K_2O	3.50	3.01	4.49	4.88	3.88	4.45	3.94	3.50	5.70	7.12	6.68	6.89	4.76
P_2O_5	0.46	0.54	0.51	0.62	0.63	0.60	0.55	0.48	0.36	0.22	0.58	0.55	0.50
LOI	0.58	1.38	0.71	0.81	0.72	0.63	0.71	1.12	1.30	1.14	1.91	1.53	1.62
Total	100.38	99.99	99.71	100.50	100.03	99.53	99.81	100.80	99.91	100.51	99.30	99.99	99.93
ppm													
Ba	548	830	1216	767	1083	1291	1192	817	659	503	906	1027	1402
Sr	490	944	810	962	919	1132	960	662	440	831	1799	1250	1211
Co	63	49	20	21	25	26	28	24	22	16	23	21	22
Ni	112	52	41	58	23	39	34	30	16	14	14	16	19
V	243	338	262	192	282	265	165	182	224	162	387	282	192
Cr	311	214	51	71	39	67	38	32	30	26	69	48	40
Rb	44	72	121	40	72	72	71	75	83	127	115	102	92
Be	0.52	0.92	1.44	0.90	0.56	0.90	1.10	1.12	1.30	1.62	1.08	1.20	1.43
Zr	32	46	56	104	68	63	79	51	58	45	45	52	74
Nb	2.40	3.32	2.49	3.70	3.33	4.15	4.72	3.30	2.45	2.84	3.06	4.12	4.50
Y	14	23	18	8	25	22	12	13	15	16	19	18	18
Mo	1.93	2.30	3.27	5.20	1.57	2.40	3.41	3.65	2.64	2.10	2.12	1.90	1.65
W	0.52	1.20	1.02	1.30	0.40	0.65	1.22	1.02	1.23	1.00	0.56	1.19	1.02
Cs	1.47	0.92	1.68	0.80	1.63	2.45	0.92	0.62	0.82	1.21	2.14	2.03	2.18
Hf	1.65	1.74	1.62	1.60	2.69	2.35	2.84	1.99	1.72	1.24	1.38	1.65	2.44
Ta	0.22	0.32	0.34	1.10	0.42	0.45	0.56	0.60	0.86	0.54	0.20	0.44	0.65
Ga	14.7	15.1	15.6	16.1	15.8	15.6	17.3	16.9	17.4	16.9	17.7	16.9	16.4
Th	1.32	1.20	1.30	1.30	2.27	2.14	2.93	1.65	0.98	1.43	1.06	1.46	2.26
U	0.42	0.47	0.72	0.70	0.75	0.61	0.91	0.72	0.68	0.75	0.43	0.63	0.82
Cu	120	159	143	105	97	103	162	138	130	110	107	112	64
Zn	32	63	82	99	54	48	100	67	82	69	176	84	32
Pb	4.0	6.1	6.4	7.1	5.5	5.2	8.1	7.4	9.2	8.2	7.4	7.1	6.8
La	5.08	4.91	8.14	7.46	13.2	12.3	13.5	12.8	9.12	8.84	15.8	15.4	14.0
Ce	11.19	13.52	15.81	18.80	28.30	29.45	16.40	14.4	17.01	18.50	23.30	18.31	14.33
Pr	2.45	2.62	2.79	2.29	4.14	4.12	2.59	2.01	1.14	2.72	2.47	2.54	2.50
Nd	10.33	12.34	12.58	8.97	15.30	17.20	6.78	5.94	5.43	11.62	11.30	10.21	11.02
Sm	3.18	3.63	3.60	2.29	5.23	4.43	2.00	2.06	2.12	3.49	2.92	3.02	3.72
Eu	0.92	1.48	1.33	0.80	1.86	1.55	0.92	0.90	0.82	1.12	1.15	1.28	1.12
Gd	2.10	3.62	3.93	2.52	4.61	4.24	2.30	1.99	1.48	3.30	3.47	3.15	3.83
Tb	0.41	0.58	0.72	0.41	0.78	0.79	0.51	0.50	0.42	0.62	0.54	0.61	0.40
Dy	3.12	4.12	3.59	2.39	4.38	3.85	2.56	2.45	2.39	3.51	3.40	3.46	4.12
Ho	0.50	0.94	0.72	0.39	0.92	0.65	0.62	0.73	0.54	0.72	0.68	0.72	0.50
Er	1.43	3.14	2.90	1.12	2.25	2.02	1.32	1.24	1.81	1.82	2.22	2.43	2.19
Tm	0.26	0.46	0.38	0.17	0.44	0.37	0.21	0.23	0.24	0.34	0.28	0.42	0.32
Yb	1.65	2.40	1.96	1.06	2.19	2.24	1.84	1.88	1.62	1.91	1.72	1.90	2.41
Lu	0.22	0.49	0.95	0.14	0.31	0.35	0.23	0.33	0.42	0.32	0.27	0.32	0.36

Table 3. Electronic microprobe analysis data for hydrothermal biotite from the Kirganik prospect (wt.%)

Sample ID	SiO_2	TiO_2	Al_2O_3	FeO	MnO	MgO	CaO	K_2O	Na_2O	BaO	Cr_2O_3	NiO	F	Cl	SO_3
Large biotite crystals associated with Cu sulfides in potassic alteration assemblage															
Core zones															
108	34.96	4.48	14.73	13.41	0.30	16.29	0.07	9.62	0.17	0.48	0.00	0.01	1.06	0.07	0.00
110	35.77	4.37	13.68	13.32	0.33	16.30	0.01	9.96	0.13	0.19	0.01	0.01	1.17	0.04	0.02
Rim zones															
110	34.80	4.88	14.44	13.93	0.31	15.53	0.02	10.00	0.22	0.50	0.03	0.02	0.98	0.05	0.00
Small biotite crystal associated with Cu sulfides in potassic alteration assemblage															
141	37.31	3.59	12.62	14.34	0.38	17.18	0.42	9.86	0.11	0.00	0.00	0.00	1.48	0.06	0.01

Table 4. Electronic microprobe analysis data for hydrothermal apatite from the Kirganik prospect (wt.%)

Sample ID	SiO_2	Al_2O_3	FeO	MnO	MgO	CaO	Na_2O	P_2O_5	BaO	SrO	Ce_2O_3	La_2O_3	F	Cl	SO_3
Large crystals and crystal aggregates with no or trace Cu sulfides (calc-potassic alteration)															
Inner (core) zones															
102	0.57	0.04	0.02	0.03	0.13	55.80	0.15	41.20	0.15	0.32	0.06	0.00	2.27	0.22	1.01
113	0.07	0.03	0.03	0.07	0.02	55.41	0.21	41.32	0.16	0.27	0.03	0.06	2.75	0.29	0.79
115	0.41	0.03	0.08	0.06	0.03	55.23	0.20	40.67	0.15	0.28	0.10	0.06	2.37	0.24	0.77
116	0.39	0.01	0.06	0.06	0.05	55.32	0.18	40.84	0.17	0.28	0.08	0.00	3.31	0.32	0.97
144	0.06	0.03	0.14	0.11	0.06	55.36	0.37	41.30	0.15	0.24	0.05	0.04	2.53	0.15	1.11
146	0.03	0.02	0.09	0.06	0.01	55.72	0.20	42.29	0.16	0.30	0.02	0.00	2.37	0.19	0.48
Outer (rim) zones															
101	0.29	0.00	0.33	0.06	0.04	55.92	0.13	41.66	0.19	0.30	0.07	0.01	2.28	0.12	0.62
103	0.38	0.02	0.17	0.07	0.02	55.42	0.20	41.36	0.15	0.30	0.07	0.04	2.34	0.12	0.81
112	0.37	0.01	0.12	0.07	0.02	55.22	0.15	41.02	0.16	0.29	0.08	0.01	2.60	0.28	0.75
114	0.26	0.01	0.09	0.06	0.04	55.66	0.17	40.89	0.16	0.26	0.08	0.04	2.19	0.24	0.59
117	0.32	0.02	0.08	0.07	0.02	55.61	0.15	41.05	0.15	0.24	0.06	0.05	3.48	0.26	0.71
118	0.37	0.01	0.07	0.05	0.02	55.40	0.11	40.79	0.15	0.28	0.05	0.02	3.28	0.31	0.82
145	0.38	0.01	0.12	0.06	0.04	55.39	0.19	41.18	0.16	0.28	0.07	0.00	2.30	0.24	0.80
147	0.38	0.03	0.08	0.04	0.03	55.84	0.16	41.60	0.18	0.29	0.08	0.01	2.28	0.22	0.61
Small crystals, crystal chains and crystal aggregates associated with Cu sulfides (potassic alteration)															
128	0.51	0.01	0.16	0.08	0.03	55.53	0.19	40.48	0.15	0.25	0.08	0.00	3.21	0.28	1.00
129	0.44	0.01	0.13	0.06	0.04	55.38	0.19	40.69	0.17	0.27	0.10	0.00	3.08	0.34	1.03
138	0.02	0.01	0.10	0.09	0.04	55.51	0.33	41.34	0.18	0.28	0.04	0.00	2.38	0.21	0.77
139	0.41	0.01	0.10	0.05	0.02	55.55	0.18	40.91	0.16	0.29	0.07	0.03	2.47	0.18	0.76
149	0.04	0.00	0.08	0.03	0.04	54.88	0.31	41.36	0.15	0.25	0.03	0.01	2.79	0.26	0.85
150	0.48	0.03	0.15	0.08	0.05	54.72	0.18	40.09	0.14	0.25	0.08	0.00	2.96	0.20	0.83
151	0.05	0.00	0.09	0.06	0.03	55.19	0.29	41.32	0.14	0.27	0.06	0.03	2.76	0.32	0.87
152	0.27	0.03	0.12	0.11	0.04	55.27	0.15	41.24	0.13	0.23	0.06	0.00	2.90	0.28	0.69
153	0.04	0.01	0.10	0.09	0.05	54.55	0.43	40.38	0.13	0.26	0.04	0.01	3.34	0.27	1.34
154	0.09	0.02	0.16	0.10	0.04	54.74	0.20	40.93	0.15	0.26	0.05	0.02	3.32	0.26	0.75

Table 5. Electronic microprobe analysis data for hydrothermal magnetite from the Kirganik prospect (wt.%)

Sample ID	SiO_2	TiO_2	Al_2O_3	FeO	MnO	MgO	CaO	NiO	V_2O_3	Cr_2O_3	ZnO
Magnetite containing small rounded bornite inclusions (calc-potassic alteration)											
170	0.18	1.28	0.27	97.08	0.02	0.02	0.03	0.02	0.30	0.02	0.00
104	0.02	1.21	0.28	95.70	0.14	0.02	0.01	0.01	1.24	0.00	0.08
105	0.14	1.37	0.23	95.77	0.22	0.05	0.03	0.06	1.23	0.04	0.09
107	0.06	1.01	0.13	97.09	0.06	0.03	0.02	0.01	1.40	0.05	0.06
Magnetite from potassic alteration assemblage associated with abundant Cu sulfides											
106	0.12	0.70	0.21	97.48	0.11	0.03	0.02	0.00	1.23	0.02	0.06
165	0.11	0.45	0.03	97.24	0.04	0.03	0.03	0.00	1.24	0.12	0.05
166	0.05	0.48	0.01	98.06	0.04	0.04	0.02	0.02	0.88	0.11	0.02
174	0.22	0.31	0.29	97.92	0.10	0.13	0.02	0.02	0.41	0.02	0.00

Table 6. Representative ICP-MS analyses of calc-potassic and potassic hydrothermal alteration assemblages from the Kirganik prospect (ppm)

	Pyroxene-K-feldspar-apatite-magnetite (calc-potassic) alteration			Biotite-K-feldspar-magnetite (potassic) alteration with Cu-sulfides						
Sample numbers	21	22	23	24	25	26	27	28	29	30
Au	0.3	0.3	0.1	0.1	0.1	0.7	0.3	1.2	1.4	0.0
Ag	0.2	0.2	0.2	1.1	0.8	4.6	2.4	11.3	12.1	0.8
Cu	268	409	398	14878	32211	12354	17147	30539	16297	1526
As	36.3	17.1	14.8	0.0	5.0	4.2	12.2	8.6	7.3	1.8
Sb	0.7	0.7	3.6	1.0	0.1	0.5	0.2	1.0	2.9	0.9
Co	75.4	99.8	79.1	7.7	34.1	15.2	29.6	29.2	17.8	18.8
Ni	30.5	42.5	31.3	13.7	9.1	11.7	5.2	7.2	13.7	14.8
Zn	256.6	345.4	283.4	19.1	62.8	28.2	61.6	43.4	36.6	110.7
Pb	4.8	4.4	5.0	6.5	10.8	35.5	8.5	16.0	17.3	13.2
Bi	0.0	0.1	0.0	1.1	0.0	9.9	0.1	3.1	0.9	0.3
Se	5.7	4.9	1.1	6.3	2.7	12.7	6.5	7.8	40.4	1.0
Te	0.0	0.4	0.0	0.7	1.9	3.5	0.2	0.7	0.5	0.2
Hg	0.1	0.0	0.0	0.4	0.0	2.8	0.1	0.5	1.0	0.2
Mo	0.5	0.3	0.2	3.2	0.7	1.8	1.4	1.3	1.2	0.6
W	3.5	0.7	2.8	7.0	2.3	1.9	1.6	4.0	3.0	0.4
Sn	1.8	1.8	1.5	0.9	0.7	0.4	0.4	0.3	0.4	0.0
Ti	12885	16512	14304	3263	2909	4144	2911	3896	2300	4435
V	1531	2383	1727	16	726	55	563	197	290	284
Cr	8.6	2.1	4.4	6.9	6.9	13.1	13.1	16.4	26.3	10.7
Mn	3636	4157	3447	190	449	337	439	450	408	1271
Cd	0.1	0.0	0.2	8.0	0.3	0.7	0.5	0.6	0.6	0.5
In	0.1	0.1	0.1	0.1	0.0	0.0	0.0	0.0	0.1	0.1
B	10.8	6.0	7.5	2.5	1.5	1.8	2.1	2.6	0.6	14.8
Ga	32.7	39.5	34.5	16.5	19.8	18.6	18.9	18.4	14.7	19.6
Ge	1.6	1.1	2.0	0.4	0.7	0.5	0.7	0.4	0.1	1.9
Zr	52.7	42.5	51.0	8.5	2.4	2.0	1.8	0.8	0.5	26.8
Nb	2.5	1.9	1.7	3.1	3.6	1.5	3.3	4.0	0.8	3.0
Hf	1.6	1.3	1.5	0.4	0.2	0.2	0.1	0.1	0.0	0.9
Ta	0.2	0.2	0.2	0.2	0.1	0.0	0.2	0.2	0.1	0.2
Be	1.1	0.9	1.3	0.3	0.2	0.1	0.3	0.2	0.6	0.7
Ba	213	139	260	2100	1629	3443	1487	1490	379	1760
Li	43.3	23.8	42.9	16.1	12.2	14.0	11.9	15.2	5.7	35.0
Rb	15.6	8.4	21.0	86.4	77.8	92.4	44.5	66.1	35.3	109.3
Sr	527	232	345	650	1366	886	1271	1131	200	2268
Cs	42.9	2.3	22.0	0.6	1.0	0.7	0.5	0.8	0.2	1.2
Th	2.3	0.8	0.1	0.1	0.1	0.0	0.2	0.0	0.1	0.4
U	0.4	0.1	0.1	0.2	0.2	0.1	0.2	0.1	0.0	0.2
Y	38.2	14.1	10.2	3.9	1.6	3.1	2.0	1.8	3.6	10.3
La	13.2	5.3	2.1	0.6	0.9	0.7	0.5	0.6	0.7	2.9
Ce	41.4	15.8	6.9	2.4	2.8	1.9	1.9	1.9	2.1	8.6
Pt*	0.02	0.00	0.01	0.00	0.00	0.00	0.00	0.02	0.00	0.02
Ru	0.00	0.00	0.05	0.06	0.14	0.01	0.13	0.03	0.06	0.00
Rh	0.01	0.01	0.00	0.14	0.33	0.14	0.20	0.30	0.15	0.01
Pd	0.77	0.68	0.56	0.33	0.04	0.62	0.18	0.19	0.11	0.77

*no Re, Os, Ir detected.

Table 7. Electronic microprobe analysis data for some Cu-sulfide minerals from the Kirganik prospect (wt.%)

Sample ID	Minerals	Au	Ag	Cu	S	Te	As	Sb	Fe	Hg	Bi	Total	Empirical form
121a	Bornite	0.00	0.07	63.26	26.92	0.00	0.00	0.02	10.17	0.04	0.00	100.47	$Cu_{4.94}Fe_{0.90}S_{4.16}$
121b	Bornite	0.00	0.01	64.62	25.85	0.00	0.01	0.00	10.32	0.00	0.00	100.81	$Cu_{5.06}Fe_{0.92}S_{4.02}$
119a	Bornite	0.00	0.06	64.09	26.05	0.00	0.00	0.00	10.59	0.00	0.00	100.80	$Cu_{5.02}Fe_{0.94}S_{4.04}$
119b	Bornite	0.04	0.01	63.35	26.08	0.01	0.00	0.01	10.92	0.00	0.00	100.41	$Cu_{4.97}Fe_{0.97}S_{4.06}$
126	Bornite	0.15	0.02	63.56	26.06	0.02	0.00	0.00	11.03	0.00	0.00	100.84	$Cu_{4.98}Fe_{0.98}S_{4.04}$
131	Bornite	0.00	0.01	64.00	26.29	0.00	0.01	0.02	11.08	0.00	0.00	101.41	$Cu_{4.97}Fe_{0.98}S_{4.05}$
158	Bornite	0.00	0.04	63.49	26.08	0.00	0.00	0.00	11.27	0.00	0.00	100.88	$Cu_{4.96}Fe_{1.00}S_{4.04}$
165a	Bornite	0.00	0.05	62.89	26.45	0.00	0.00	0.01	11.34	0.00	0.00	100.73	$Cu_{4.91}Fe_{1.00}S_{4.09}$
165b	Bornite	0.05	0.05	62.80	26.30	0.00	0.00	0.02	11.34	0.00	0.00	100.56	$Cu_{4.91}Fe_{1.01}S_{4.08}$
166	Bornite	0.09	0.04	61.26	27.51	0.00	0.02	0.00	12.42	0.00	0.00	101.33	$Cu_{4.72}Fe_{1.08}S_{4.2}$
168	Bornite	0.00	0.00	59.99	26.69	0.00	0.00	0.04	14.12	0.00	0.12	100.98	$Cu_{4.65}Fe_{1.25}S_{4.1}$
172	Bornite	0.00	0.02	54.57	30.20	0.00	0.02	0.00	15.65	0.00	0.17	100.63	$Cu_{4.13}Fe_{1.34}S_{4.53}$
173	Bornite	0.00	0.00	57.78	29.04	0.03	0.03	0.07	13.55	0.01	0.05	100.55	$Cu_{4.42}Fe_{1.18}S_{4.4}$
175	Bornite	0.00	0.00	60.53	26.21	0.06	0.00	0.03	14.36	0.00	0.10	101.29	$Cu_{4.70}Fe_{1.27}S_{4.03}$
123	Chalcopyrite	0.00	0.01	35.33	34.87	0.02	0.00	0.00	28.84	0.00	0.00	99.06	$Cu_{1.03}Fe_{0.96}S_{2.01}$
168	Chalcopyrite	0.00	0.02	35.63	34.88	0.00	0.00	0.01	29.31	0.00	0.00	99.85	$Cu_{1.03}Fe_{0.97}S_{2.00}$
109	Chalcopyrite	0.00	0.03	34.49	35.92	0.01	0.00	0.01	30.48	0.00	0.00	100.94	$Cu_{0.98}Fe_{0.99}S_{2.03}$
169	Chalcopyrite	0.00	0.01	35.92	32.34	0.04	0.01	0.00	30.08	0.00	0.10	98.49	$Cu_{1.07}Fe_{1.02}S_{1.91}$
171	Chalcopyrite	0.00	0.08	34.04	34.42	0.00	0.00	0.00	30.72	0.00	0.16	99.41	$Cu_{0.99}Fe_{1.02}S_{1.99}$

Table 8. Electronic microprobe analysis data for native gold from the Kirganik prospect (wt.%)

Sample ID	Au	Ag	Cu	Hg	Te	As	Bi	Sb	Fe	Pt	Pd	T
121	89.82	3.26	5.83	0.35	0.00	0.02	0.00	0.00	0.67	0.00	0.00	9
124	90.20	4.44	3.55	0.17	0.06	0.00	0.13	0.07	0.54	0.01	0.26	9
172	89.57	7.86	0.94	0.58	0.03	0.01	0.00	0.00	0.92	0.00	0.00	9

Table 9. Analytical data of Rb-Sr isotope ratios and Rb-Sr contents in minerals and whole rock samples from potas alteration assemblages at the Kirganik prospect

Sample ID		Fraction	Rb, ppm	Sr, ppm	$^{87}Rb/^{86}Sr$	± 2σ	$^{87}Sr/^{86}Sr$	± $2\sigma_m$
1	31	Biotite	254.0	71.6	10.277	0.103	0.714003	0.000016
2		K-feldspar	169.8	1625.0	0.302	0.003	0.703629	0.000018
3	32	Biotite	244.3	82.9	8.506	0.085	0.712162	0.000017
4		K-feldspar	125.9	1554.6	0.234	0.002	0.703566	0.000017
5	33	Whole rock*	121.0	2022.3	0.286	0.003	0.703617	0.000016

* Pyroxene 40 vol.%, K-feldspar 50 vol. %, biotite 10 vol.%

Table 10. Types of fluid inclusions (FI) in minerals from various hydrothermal assemblages at the Kirganik prospe

Mineral (number of FI studied)	FI type	FI size, µm	FI content	T_m eu., °C	T_m ice, °C	Homogenization, T_h, °C	Estimated salinity, wt.% [a]	Estima pressur (entrapm temperat
Pyroxene-K-feldspar-apatite-magnetite (calc-potassic) alteration								
Apatite – 1 (25)	1	<5-30	35 vol.% gas	-45.5 to -44.0	-6.5 to -7.0	To liquid: gas at 335-345	10	2.2 kba (550 °C
Biotite-K-feldspar-magnetite (potassic) alteration with Cu-sulfides								
Apatite – 2 (15)	2	<5-20	20 vol.% gas	-33.5 to -32.5	--3.0 to -3.5	To liquid: gas at 270-280	5	2.1 kba (450 °C

T_m eu. – eutectic temperature (first melting temperature), °C; T_m ice - final ice melting temperature, °C;
[a]Salinity was estimated by final ice melting temperatures for the NaCl-H_2O system (Bodnar and Vityk, 1994);
[b]The trapping pressure estimated by using the salinity of fluid inclusions, homogenization temperature (T_h), and the temperature of mineral format (trapping temperature) defined by mineral paragenesis (Roedder 1984; Bodnar and Vityk 1994).